AN INTERFERENCE-CANCELLATION RECEIVER FOR MULTI-BAND AND MULTI-STANDARD WIRELESS COMMUNICATION SYSTEMS

A Dissertation
Presented to
The Academic Faculty

by

Sungho Beck

In Partial Fulfillment
Of the Requirements for the Degree
Doctor of Philosophy in the
School of Electrical and Computer Engineering

Georgia Institute of Technology
August 2011

AN INTERFERENCE-CANCELLATION RECEIVER FOR MULTI-BAND AND MULTI-STANDARD WIRELESS COMMUNICATION SYSTEMS

Approved by:

Dr. Emmanouil M. Tentzeris, Advisor
School of Electrical and Computer Engineering
Georgia Institute of Technology

Dr. Kevin T. Kornegay
School of Electrical and Computer Engineering
Georgia Institute of Technology

Dr. Shyh-Chiang Shen
School of Electrical and Computer Engineering
Georgia Institute of Technology

Dr. Chang-Ho Lee
School of Electrical and Computer Engineering
Georgia Institute of Technology

Dr. Jun-Hee Heu
School of Electrical Engineering and Computer Science
Seoul National University

Date Approved: June 22, 2011

ACKNOWLEDGEMENTS

I cannot begin to express my thanks to Holy God, who has been guiding throughout my life. I'm deeply indebted to my research advisor, Professor Manos M. Tentzeris. Without his guidance, I would not have achieved this research goal. I am also grateful to all the committee members, Professor Chang-Ho Lee, Professor Kevin T. Kornegay, Professor Shyh-Chiang Shen, and Dr. Jun-Hee Heu for their time and effort in reviewing my dissertation and serving as my defense committee members.

I would like to thank to Dr. Joy Laskar, Dr and Kyetae Lim for their great support and guidance. I also wish to thank my colleague members in Microwave Application Group for making good environment. I'd also like to extend my gratitude to the Samsung Design Center and Future Communication ICs Inc., Korea for their numerous supports and advices. I cannot leave Georgia Tech without mentioning friends in Saehan church—in particular Prof. Jeongsik Lee and Seoul Science High School who have always made my Atlanta life happier throughout the doctorate program.

And most of all, I would like to deepest appreciation to my parents, Donghyun Beck and Jungock Park, and my parents-in-law, Pyungshup Noh and Kyungshin Woo, for their incomparable love. Word cannot express my love and appreciation to family, Hyekyoung Noh, Jongwoo, and Nathan – they are treasure of my life.

TABLE OF CONTENTS

LIST OF TABLES

LIST OF FIGURES

SUMMARY

Along with the tremendous popularity of wireless mobile communications, the demand for multiple functionality in multiple frequency bands has been growing. As a result, a multi-standard multi-band wireless receiver has gained high attention. The wideband code-division multiple access (WCDMA) system has been widely used for the third-generation wireless communication system. It has an ability to receive and transmit data between a base station and a mobile terminal at the same time. Because of this full duplex, the strong transmitting signal distorts the weak receiving signal. As a result, passive standing wave (SAW) filters becomes necessary for the radio frequency (RF) front end, but they cannot be integrated into a silicon chip. One result is that SAW filters have become a bottleneck in multi-band multi-standard receivers. The dissertation presents novel methodologies to overcome this bottleneck. First, the receiver specifications are derived from the wireless communication standard. These specifications are then used to obtain the required amount of TX leakage cancellation by using a proposed frequency selective feedback topology with multi-band capability. The effectiveness of this technique is demonstrated by the measurement of prototype integrated circuit (IC). To make the IC operate for multi-standard, another novel technique is also proposed for a channel-selection filter. With a proposed interpolated resistor bank, the active-RC channel-selection filter has programmable gain and pseudo-continuous bandwidth, which reduce the total power consumption and silicon area of the receiver. The measured result of a prototype silicon chip shows the effectiveness of the technique. With these two topologies, a multi-band multi-standard receiver that uses low power can be realized at a cost.

CHAPTER 1
INTRODUCTION

1.1 MOTIVATION

Diversified wireless communication standards have been introduced to mobile terminals, and as a result, demands for multi-band and multi-standard chipsets are rapidly increasing. For example, cellular communication technology such as wideband code-division multiple access (WCDMA), wireless local area network, Bluetooth®, and mobile-TVs can be integrated into a single phone. WCDMA has been accepted as the global third generation communication standard. Meanwhile, mobile-TVs such as digital video broadcasting-handheld (DVB-H) and terrestrial digital multimedia broadcasting (T-DMB) are considered as key applications for the near future. Therefore, the effective integration of WCDMA and mobile-TVs is required.

As many functions are integrated into a single piece of mobile equipment, cost and printed circuit board (PCB) area should be minimized. In addition, to lengthen operating time of a mobile device, low-power consumption has been first priority of mobile chipsets. Due to improvements in the complementary metal-oxide semiconductor (CMOS) process and digital-signal processing (DSP) technology, digital-baseband chips are ready to support multiple standards without introducing significant penalties of cost, PCB area, or power consumption. However, because radio-frequency (RF) transceivers conventionally adopt individual components to meet the stringent requirements of each standard, they cannot take advantage of the CMOS process scaling. Developing a multi-band and multi-standard receiver with low cost and low-power consumption requires

solving the following problems. First, whenever additional bands are supported by a transceiver, additional external receive (RX) and/or transmit (TX) filters should be used as shown in Figure 1. It requires additional cost and PCB area. Second, since the bandwidth of a channel-selection filter (CSF) should be adjusted to each standard, it is hard to integrate the CSF into a small silicon area and merge it with a programmable-gain amplifier (PGA). Therefore, the cost and the power consumption increases for multi-standard operations. As a result, the transceiver becomes a bottle-neck for a multi-band and multi-standard mobile terminal.

One way to achieve low-cost, low-power, and small mobile equipment for multi-band and multi-standard wireless communication systems is to develop a novel transceiver by introducing innovative CSFs, LNAs, and mixers.

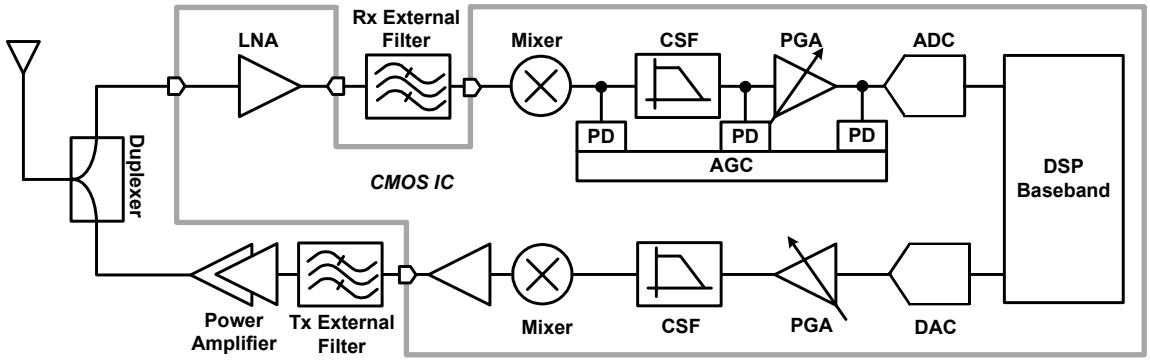

Figure 1. Block diagram of a conventional direct-conversion transceiver.

1.2 ORGANIZATION

In Chapter 1, the introduction of the dissertation demonstrates the necessity of the multi-band multi-standard SAW-less receiver, then describes the organization of the dissertation.

Chapter 2 investigates the origin of the problem and explains previous researches indicating the advantages and disadvantages of each technique.

Chapter 3 presents a detailed description of the channel-selection filter for multi-standard application. It then describes the design procedure using a top-down methodology from the system level design to the physical implementation and measurement. A novel resistor division method is proposed to obtain programmable gain for the filter, and the effectiveness of the method is demonstrated by the measurement.

Chapter 4 focuses on a radio frequency front-end design for the TX cancellation receiver for multi-band application. The chapter starts by analyzing receiver specifications derivation from the WCDMA standard. Then, the required amount of the TX leakage cancellation is derived based on the receiver specifications. To achieve the required amount of the TX leakage cancellation, a new frequency conversion feedback technique is proposed along with the phase rotate method for the multi-band applications. The measurement result demonstrates the effectiveness of the proposed techniques.

Chapter 5 summarizes the dissertation and suggests possible future research directions.

CHAPTER 2

BACKGROUND

2.1 A CHANNEL-SELECTION FILTER FOR MULTI-STANDARD APPLICATIONS

2.1.1 Specifications for multi-standard wireless communication systems

Each wireless communication standard specifies its RF performance requirements to maintain the high quality of the communication system. Table 1 summarizes several specifications for WCDMA, DVB-H, and T-DMB [1]-[3]. Figure 2 shows the measurement conditions for the adjacent channel selectivity (ACS) specifications for the DVB-H standard. To support multi-standard wireless communication systems, a channel-selection filter (CSF) confronts important challenges.

Table 1. Diversified specifications of WCDMA, DVB-H, and T-DMB

	Unit	WCDMA	DVB-H	T-DMB
Channel BW	MHz	3.84	6 / 7 / 8	1.5
Sensitivity	dBm	-106.7	-92.8 / -92.1 / -91.6	-95
Max. signal	dBm	-25	-18	-35
Dynamic range	dB	81.7	74.8	60
ACS	dB	41	29	30
Far-off selectivity	dB	60	40	40

* WCDMA: band-I
* DVB-H: L-band (1.4~1.7 GHz), modulation=16 QAM, code rate=1/2

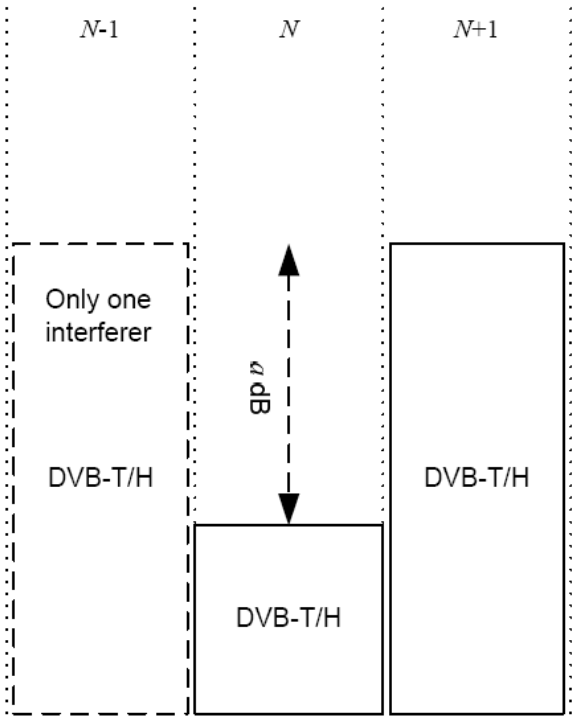

Figure 2. ACS measurement condition for DVB-H.

2.1.1.1 A widely adjustable bandwidth with fine resolution

Because channel bandwidths vary widely and unevenly as shown in Table 1, the CSF has to support widely-adjustable bandwidths with fine resolution.

2.1.1.2 A wide gain range with an adequate gain step

As a more than 80-dB variable gain range and a 40-dB adjacent-channel interferer-rejection capability are demanded of a receiver as shown in Table 1, the receiver distributes the variable gain to signal-processing blocks and optimizes the signal level by an automatic gain-control (AGC) block. To relax the dynamic range requirement of a subsequent programmable gain amplifier (PGA) as shown in Figure 1, the CSF gain needs to be adjusted widely in small steps.

2.1.1.3 Power-consumption optimization according to the existence of interferers

Low noise is required when the wanted signal is weak, whereas high linearity is demanded when large interferers exist. Both the low noise and the high linearity require high power consumption. However, these two requirements do not always occur at the same time. Therefore, power consumption can be reduced by independent control of the noise and of the linearity of the CSF.

2.1.2 The achievement of prior works

Because of its superior linearity to other topologies such as gm-C and MOSFET-C, the active-RC topology has been widely adopted for receivers in wireless communication systems [4]-[6]. The advantages and the drawbacks of prior works are described as follows.

2.1.2.1 Amir-Aslanzadeh's CSF [4]

The bandwidth of Amir-Aslanzadeh's CSF was tuned as follows: First, coarse tuning was performed by a capacitor bank as shown in Figure 3(c). Then, the bandwidth was accurately adjusted by the proposed continuous impedance multiplier (CIM) as shown in Figure 3(d). The principle of the CIM is to multiply the impedance by changing the amount of the attenuation by a potentiometer implemented using MOSFETs. The continuous bandwidth tuning is one of its advantages. One drawback is that it cannot have the ability of the gain change.

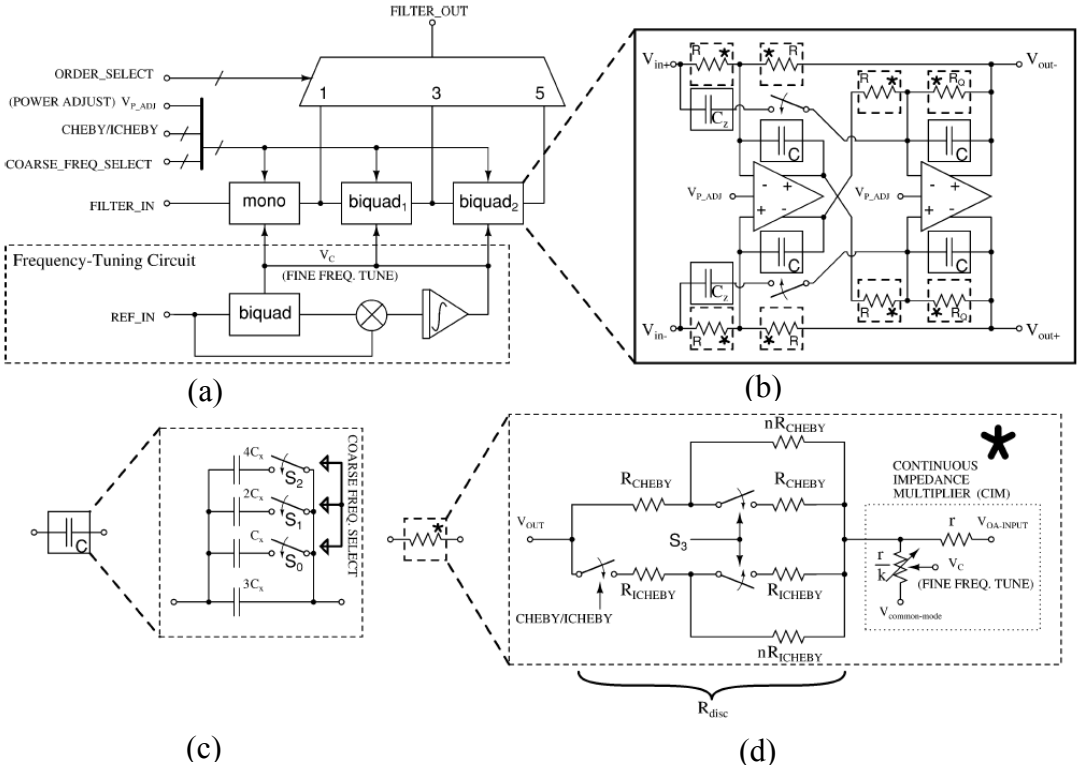

Figure 3. Amir-Aslanzadeh CSF [4] (a) top-level filter architecture, (b) biquad, (c) capacitor bank for coarse tuning, (d) resistor bank for filter type selection followed by continuous impedance multiplier.

2.1.2.2 Vasilopoulos's CSF [5]

The authors used capacitors to choose bandwidth between 5 MHz and 10 MHz as shown in Figure 4(c). Then, the fine tuning was done by a resistor bank as shown in Figure 4(d). However, as only a small portion of the total resistance was changeable, the CSF gain could not be changed.

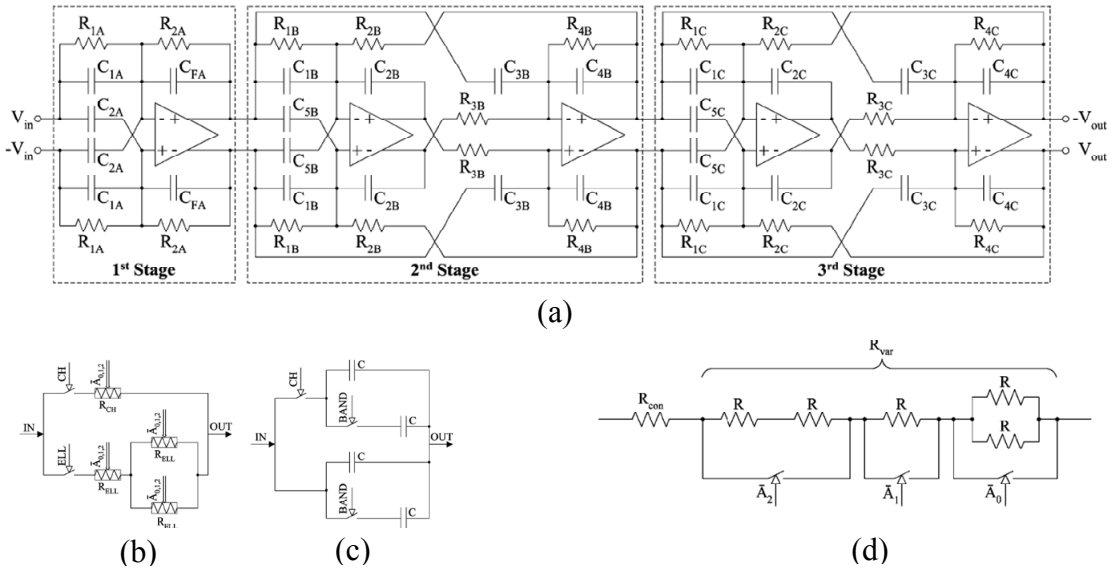

Figure 4. CSF of Vasilopoulos [5] (a) top-level filter architecture, (b) resistor array for CSF type selection, (c) capacitor bank for CSF type selection and coarse tuning, (d) potentiometer for fine bandwidth tuning.

2.1.2.3 Ozgun's CSF [6]

A CSF reported in [6] has two functions. The first function is the capability to reduce power consumption by using the proposed dynamic-impedance scaling technique, and the second function is the capability to change its gain in two 24-dB steps. Power consumption as reduced when the CSF used low current for operational trans-conductance amplifiers (OTAs) in a good signal-to-noise ratio (SNR) environment as

shown in Figure 5(b). However, simultaneously changing the input-stage current and the output-stage current did not independently optimize the noise and the output swing. In addition, 24-dB gain steps were achieved by introducing an additional PGA inside the CSF as shown in Figure 5(a). Therefore, the CSF did not actually merge PGAs neither reduce power consumption or silicon area. Indeed, the 24-dB step was too large to relax the requirements of the subsequent PGAs.

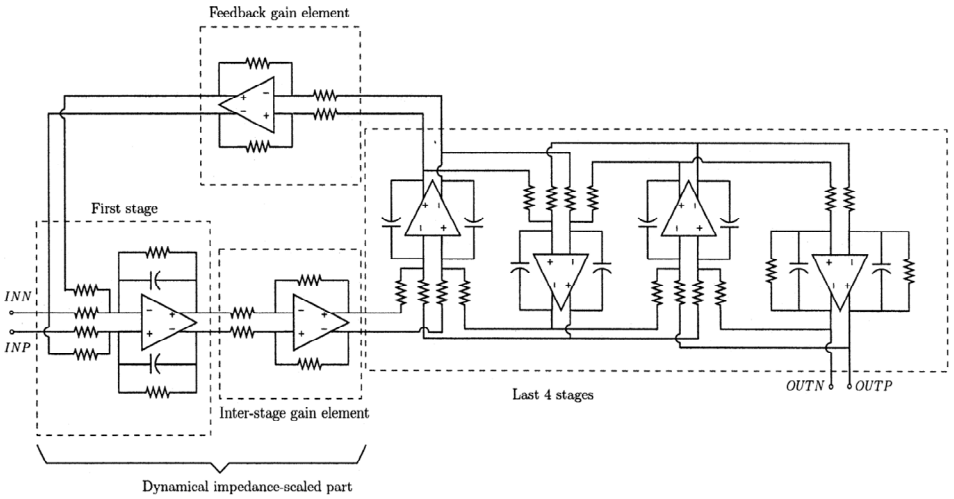

(a)

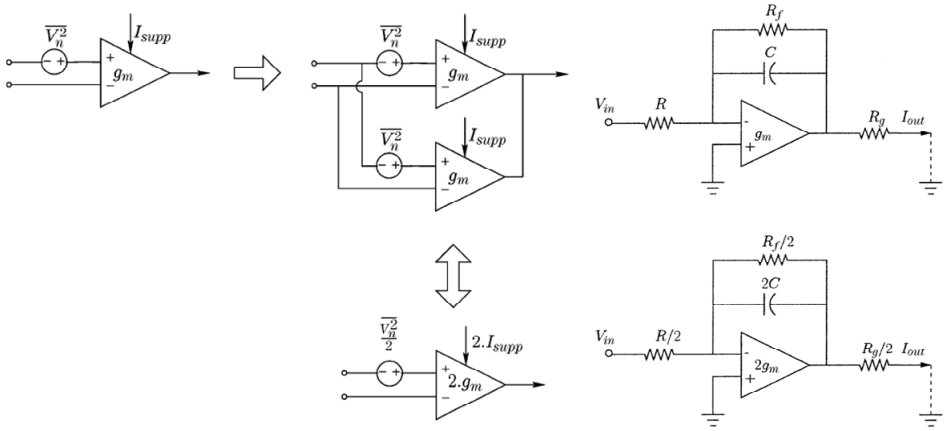

(b)

Figure 5. CSF of Ozgun [6] (a) top-level filter architecture, (b) dynamic impedance-scaling technique for power consumption and noise reduction.

2.2 AN INTERFERER-CANCELLATION RF FRONT-END FOR MULTI-BAND APPLICATIONS

2.2.1 Influences of the transmitter leakage to receiver performance

For the communication between mobile terminals and base stations, the WCDMA standard adopts frequency-division duplex (FDD) with the RX and TX frequency assignment as shown in Table 2 [1].

Table 2. Frequency assignment of WCDMA standard

Band	TX frequency (MHz)		RX frequency (MHz)		Duplex frequency (MHz)
	Min	Max	Min	Max	
I	1920	1980	2110	2170	190
II	1850	1910	1930	1990	80
III	1710	1785	1805	1880	95
IV	1710	1755	2110	2155	400
V	824	849	869	894	45
VI	830	840	875	885	45
VII	2500	2570	2620	2690	120
VIII	880	915	925	960	45
IX	1749.9	1784.9	1844.9	1879.9	95
X	1710	1770	2110	2170	400
XI	1427.9	1452.9	1475.9	1500.9	48
XII	698	716	728	746	30
XIII	777	787	746	756	31
XIV	788	798	758	768	30
XIX	830	845	875	890	45

Since a strong TX signal coexists in the FDD system, a duplexer needs to be used to isolate a weak RX signal from the strong TX signal as shown in Figure 6.

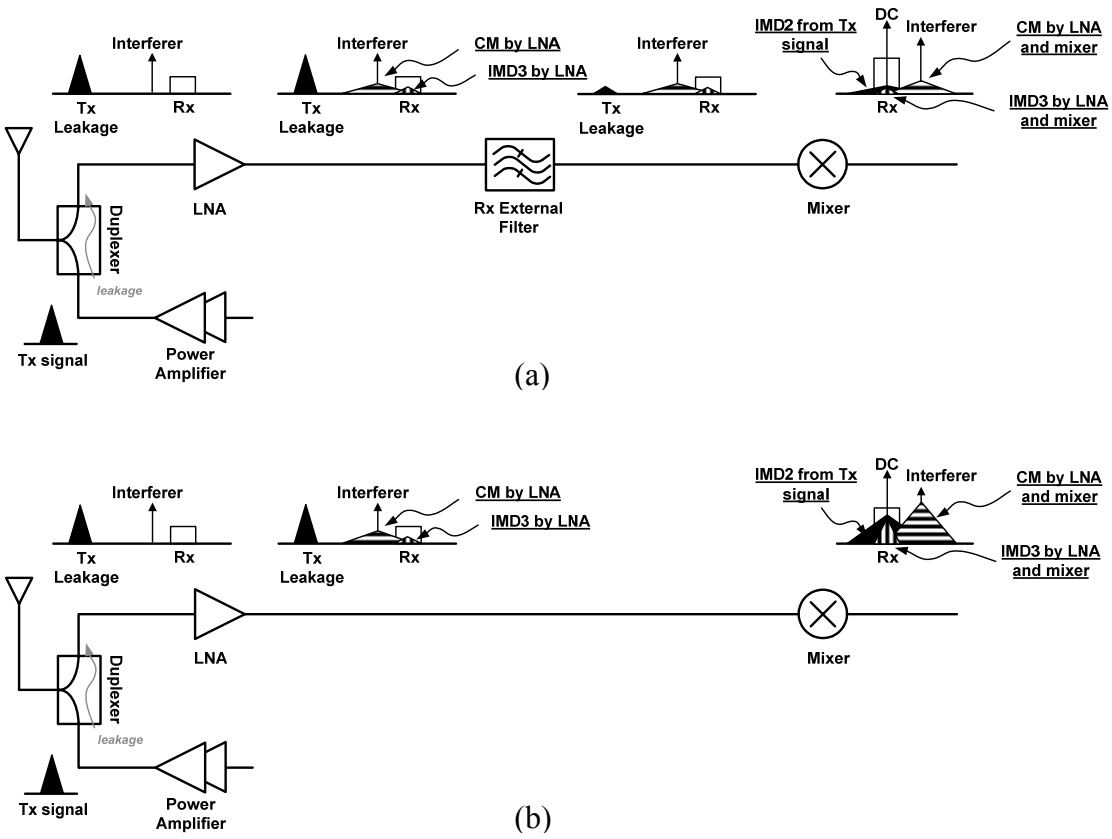

Figure 6. Scenarios of RX SNR degradation due to IMD2, IMD3, and CM (a) with RX external filter, (b) without RX external filter.

However, because of limited isolation between the TX port and the RX port of the duplexer, TX leakage exists at the LNA input. The isolation between the RX port and the TX port of a typical film bulk acoustic resonator (FBAR) is about 50-dB as shown in Figure 7 [7]. In addition, other interferers may arrive at the antenna. As the TX leakage and the interferers can distort the weak RX signal as Figure 6, the TX leakage should be attenuated. The major distortion mechanisms are explained as follows.

2.1.1.1 Second-order inter-modulation (IMD2)

The second-order distortion of the modulated TX leakage in the mixer generates disturbance around the DC frequency, where the RX signal is down-converted. If the TX leakage is not attenuated before it reaches the mixer, the second-order linearity performance of the mixer should be exceptionally high.

2.1.1.2 Third-order inter-modulation (IMD3) or cross-modulation (CM)

Both distortions originate from third-order nonlinearity. The difference is the frequencies of the RX signal, the TX leakage, and the interferer. When an interferer (or the TX leakage) is placed in the middle of the RX signal and the TX leakage (or the interferer), the IMD3 falls at the RX frequency. Otherwise, when the interferer is place near the RX signal in the cross-modulation (CM) case, the TX leakage modulates the interferer. Then, the modulated interferer degrades the SNR of the RX signal. Without TX leakage attenuation, the third-order nonlinearity requirement of the mixer becomes extremely stringent.

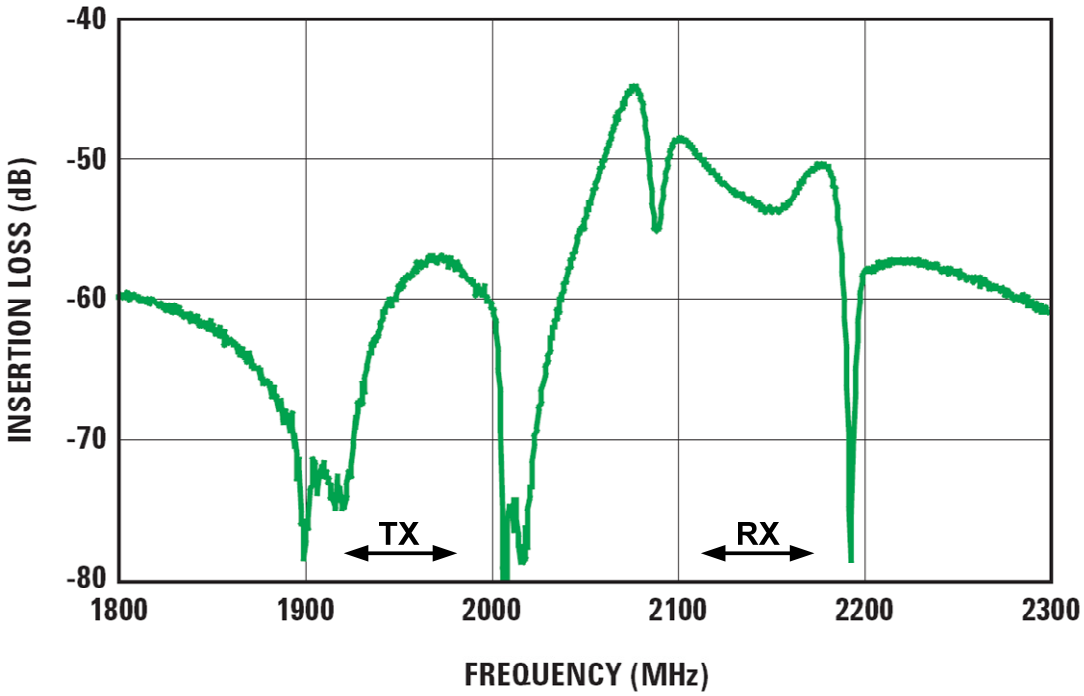

Figure 7. Isolation between the RX and TX ports of FBAR duplexer [7].

Because of the low quality factor (Q) of integrated inductors and capacitors, an on-chip LC filter cannot attenuate the TX signal enough while maintaining low loss for the RX signal. Instead, as shown in Figure 6(a), a standing acoustic wave (SAW) filter has conventionally been used between the LNA and the mixer. Low loss and high selectivity—2-dB insertion loss and 32-dB TX band attenuation—can be achieved by the SAW filter whose characteristics are dependent on the cut of the crystal and the physical dimension of the filter as shown in Figure 8 [8].

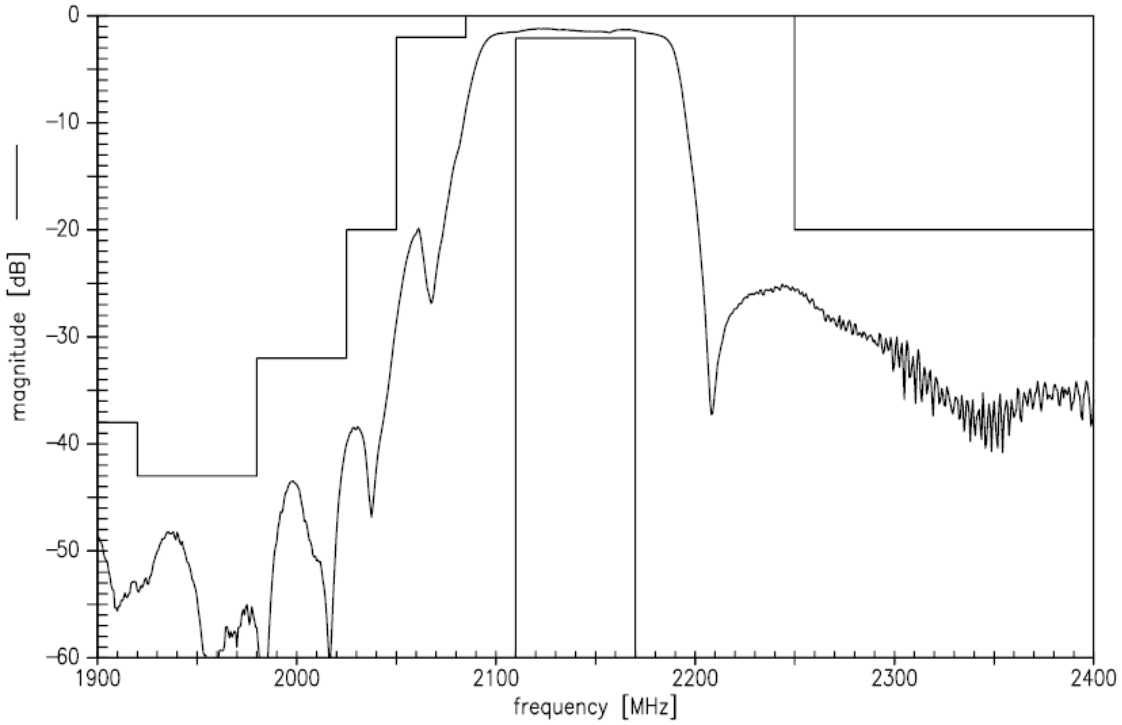

Figure 8. Typical frequency response of a WCDMA SAW filter [9].

Unfortunately, since this excellent performance is possible only by utilizing piezoelectric material, SAW filters cannot be integrated with a silicon-based transceiver. In addition, a SAW filter requires discrete components to match the transceiver impedance. Therefore, SAW filters and their associated matching elements are obstacles of small low-cost mobile devices. As more frequency bands tend to be integrated into a single transceiver, this problem will become worse. To remove SAW filters, many research studies have been carried out.

2.2.2 Research in prior works on removing SAW filters

2.2.2.1 Darabi's feed-forward cancellation [10]

Darabi's feed-forward cancellation technique utilized an RX translation loop to obtain a high Q in low-frequency domain as shown in Figure 9. After the RX signal is tapped at the LNA input, it is converted to DC frequency with a mixer. Then, the wanted RX signal is attenuated by a high-pass filter (HPF). The result was that only blockers remained at the HPF output. Finally, the blockers were up-converted to the original frequency and became null at the LNA output from the feed-forward cancellation. As a result, since the HPF bandwidth could be low regardless of the RF frequency, a high-Q RF band-pass filter (BPF) was realized at the LNA output. However, one of the drawback is that this technique required matching between the main path and the RX translation loop.

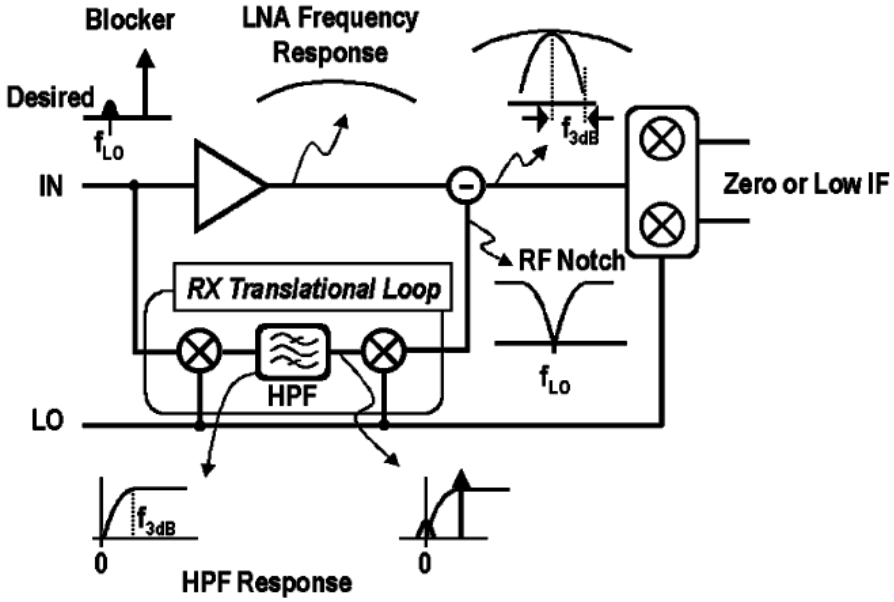

Figure 9. Feed-forward interference cancellation block [10].

2.2.2.2 Khaiti's TX signal sink at mixer outputs [11]

In widely used direct-conversion receivers, trans-impedance amplifiers (TIAs) following passive mixers, as shown in Figure 10(a), produces large distortion due to the TX leakage. To solve this problem, the authors proposed the used of a sink that has low impedance at the duplex frequency. In this way, the proposed sink absorbs the TX leakage, as a result the linearity of the TIAs was improved. In contrast, the sink had high impedance at DC, so the wanted signal was not attenuated. This technique was possible because the TX leakage was located at tens of megahertz apart from RX signals as shown in Table 2. Khaiti's sink consisted of a mixer with a LO signal with the duplex frequency and a TIA as Figure 10(b). Its frequency response is illustrated in Figure 10(c). However, this technique has drawbacks such as the requirement of additional LO signals and highly linear mixers in the RX signal path.

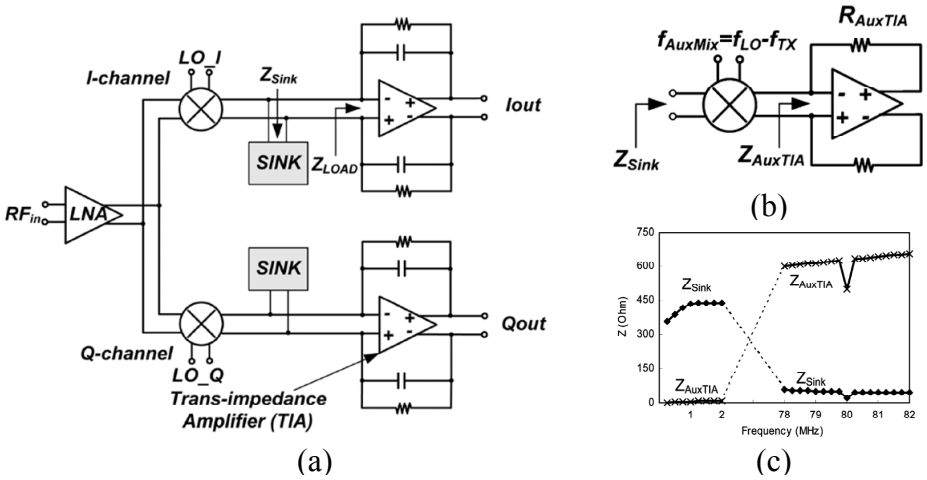

Figure 10. TX signal sink at mixer outputs [11] (a) block diagram, (b) realization of the sink, (c) impedance of the sink versus frequency.

2.2.2.3 Aparin's feedback cancellation [12]

Aparin's feedback cancellation was similar to the Darabi's feed-forward cancellation, using all of the following: down-conversion to DC, filtering, up-conversion to the original frequency, and cancellation. However, Aparin's differed in three ways. First, as it used feedback instead of the feed-forward, it was immune to the process, voltage, and temperature (PVT) variation. Second, the frequency response of Aparin's is notch while that of Darabi's is bandpass. Finally, it utilized TX LO signals that were already available from TX blocks.

However, Aparin's proposed technique had a critical problem in that it connects the feedback loop to the junction of a LNA input and the RX port of a duplexer. The RX port impedance of a duplexer is indeterminate at the TX frequency. As a result, the feedback loop characteristic was also uncertain. This issue will be addressed in following chapters.

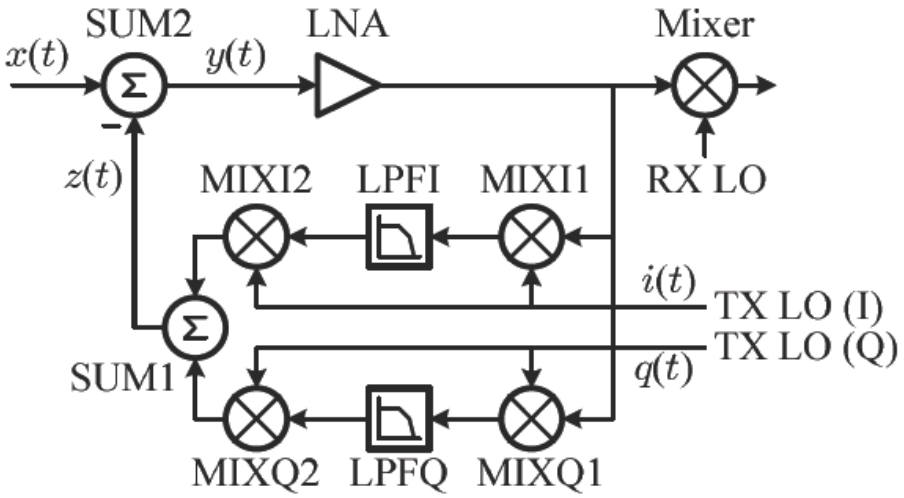

Figure 11. Block diagram of TX cancellation using feedback [11].

CHAPTER 3

AN ACTIVE-RC FILTER FOR MULTI-STANDARD

3.1 INTRODUCTION

As we have investigated in the section 2.1, a CSF for multi-standard applications has to cover a wide frequency tuning range with pseudo-continuous steps and to have a programmable gain with fine gain steps. In addition, low-power consumption is preferred to lengthen talk time. In this section, an active-RC CSF satisfying these requirements is presented.

3.2 SYSTEM LEVEL DESIGN

The Chebyshev-I topology was chosen for the CSF because it has a sharp transition band and large attenuations at stop bands. In order to control the gain of the CSF easily by changing R_{11}, R_{21}, and R_{31} without disturbing the transfer function, cascaded three Tow-Thomas biquads (BQs) [13], [14] were used in realizing the 6th order in Figure 12(a), (b) as

$$\frac{V_{out}}{V_{in}} = \prod_{n=1}^{3} \left(\frac{R_{n2}}{R_{n1}} \frac{\dfrac{1}{R_{n2}R_{n3}C_{n2}C_{n4}}}{s^2 + s\dfrac{1}{R_{n4}C_{n4}} + \dfrac{1}{R_{n2}R_{n3}C_{n2}C_{n4}}} \right). \quad (1)$$

Because the noise and the linearity of the CSF were optimized by properly allocating the pass-band gain of each BQ, the maximum gains of 1st, 2nd, and 3rd BQs were designed as 24, 6, and 0 dBV/V, respectively. Because less than unity gain is not practical, the optimized gain control ranges of 1st and 2nd BQs were 24 dB and 6 dB, respectively.

A pre-amplifier was used to increase gain between a mixer and the CSF. The DC offset compensation block was realized to prevent the saturation of the CSF due to the offset voltage using a servo loop as Figure 12(a). In addition, the bandwidth of the CSF was calibrated to desired value against the PVT variation by a bandwidth calibration block in Figure 12(c). Each block will be described in detail in the following sections.

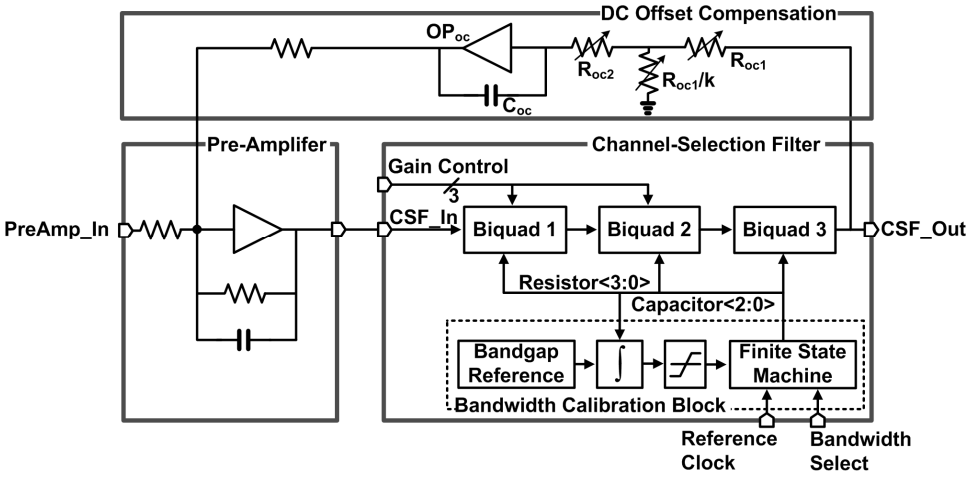

(a)

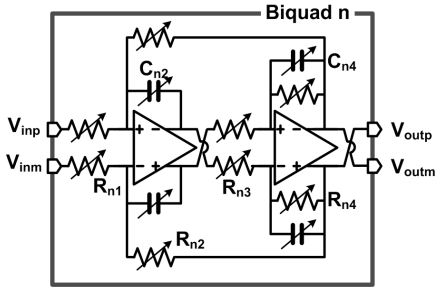

(b)

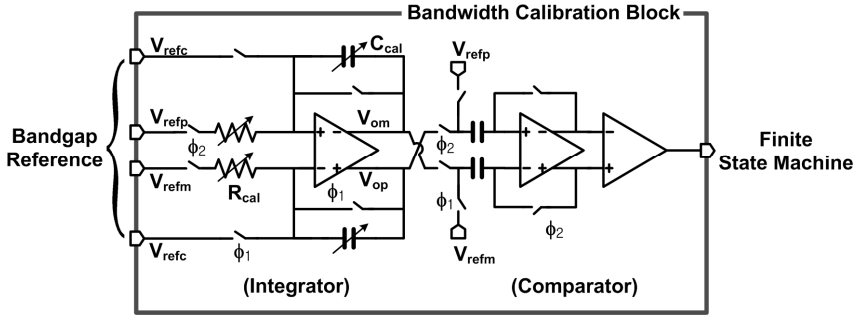

(c)

Figure 12. CSF schematic (a) block diagram, (b) biquad schematic, (c) bandwidth calibration circuit.

3.3 BINARY INTERPOLATED RESISTOR BANK

A switched resistor network, the binary interpolated resistor bank (BIRB), is proposed to achieve both the pseudo-continuous bandwidth tuning and the fine gain steps simultaneously as shown in Figure 13. The BIRB consists of a fixed resistor of $4R_u\ \Omega$, binary weighted resistors interpolated by four $2^kR_u\ \Omega$, and switches that connect the resistors.

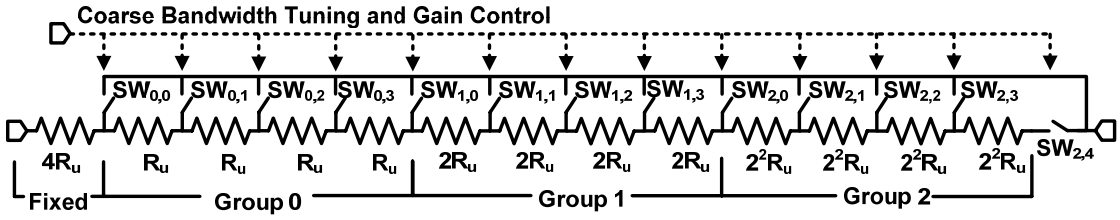

Figure 13. Binary interpolated resistor bank

If only one switch, $SW_{i,j}$, is connected and its resistance is negligible, the resistance of the BIRB is described as

$$R_{i,j} = 2^i\left(4+j\right)R_u, \tag{2}$$

where the subscripts *i* and *j* stand for the selected group and the used resistor, respectively.

An interesting property of the BIRB is that the resistance becomes double for every increment of code *i* regardless of code *j*. This property was effectively used to control the gain of the CSF by changing code *i* of R_{11} and/or R_{21} even if the exact resistance was unknown, as described below. First, the proper codes (*i, j*) for all BIRBs

were determined to roughly tune the bandwidth. Then, the bandwidth was tuned to the accurate value by changing the capacitor code with the resolution of the capacitor bank of 5 %. Finally, the gain of the CSF was adjusted by increasing or decreasing code *i* of only R_{11} and/or R_{21}. With this procedure, the 6-dB gain step was achieved even if the BIRB code (*i, j*) was unknown.

Because of the BIRB architecture, the active-RC filter obtained several important features. First, the 6-dB gain step was accomplished regardless of the bandwidth under any PVT condition. Second, as the capacitor bank needed to cover the BIRB step, only 25 %, a fine bandwidth resolution of 5 % was achieved with the 3-bit control. Therefore, because the area of the capacitor is much larger than that of the resistors, the silicon area was reduced by eliminating capacitor redundancy at the cost of introducing resistor redundancy. Finally, because all of the resistors in a BIRB consisted of well-matched integer multiples of unit resistors, the gain-step variation due to the resistor mismatch was minimized.

The reason of the silicon area reduction can be described as follows. To reduce silicon area by using small capacitance, an active-RC filter with a wide bandwidth-tuning range calls for resistor control. Three methods of the control are possible and they are compared in Table 3: continuous, segments, and the proposed methods. First, if we can choose an pre-determined resistor code for each bandwidth using the continuous resistor control method, although it is almost impractical to control the resistance continuously, capacitor banks have to cover the PVT variations of the resistor and the capacitor, ±21 % and ±15 %, respectively. Therefore, the capacitor bank requires ±36-% coverage and it requires 4-bits control for the 5-% resolution. Second, if we divide resistors into 12-

segments which are the same number of the segments as the proposed method and use one segment for each bandwidth, the capacitor bank needs to have a range of ±52.4-% with 5-bits control to cover the PVT variation and the discontinuity of the resistor values. These wide ranges of the capacitor bank, which implies large silicon area, stem from the fact that the resistor code is pre-determined for a wanted bandwidth. In contrast, as the proposed method finds proper resistor values by the calibration block, the capacitor bank only need to cover the step of the resistor bank, ±12.5 % with 3-bits control. The frequency response and the gain control of the CSF are plotted in Figure 14 as changing the BIRB code, and it shows effectiveness of the proposed method.

Table 3. Comparison of three resistor control methods

Resistor control method	Capacitor bank range	Capacitor bank bits
Continuous	±36 %	4
12 segments	±52.4 %	5
Proposed Method	±12.5 %	3

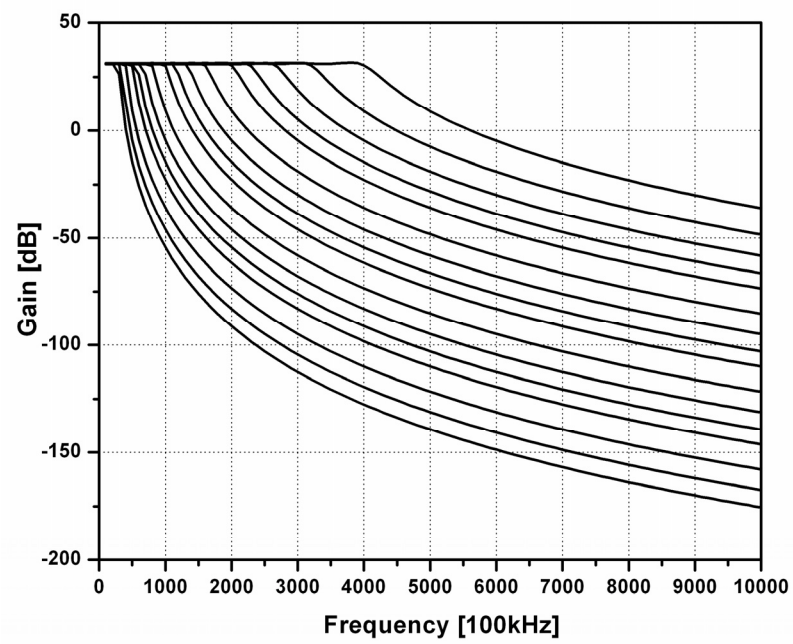

(a)

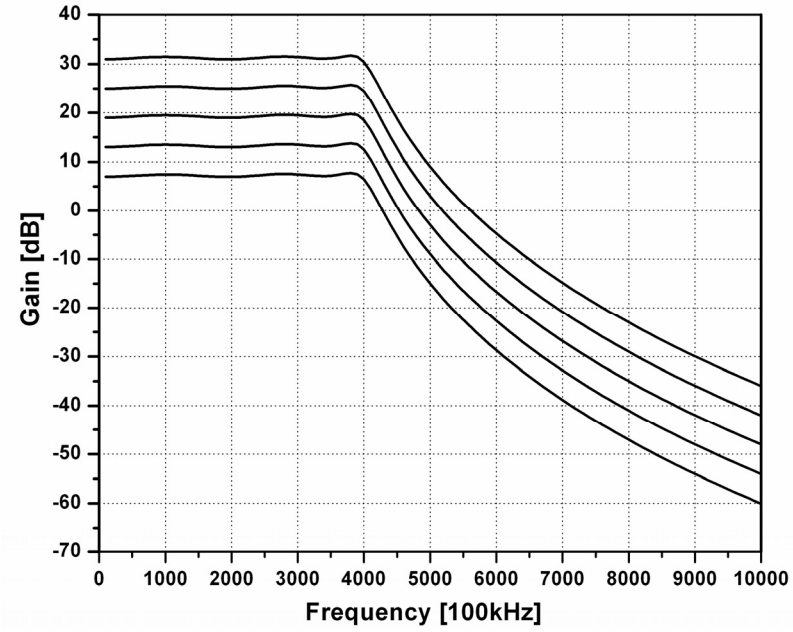

(b)

Figure 14. CSF simulation results when only resistors are changed (a) frequency response, (b) gain control.

3.4 PROPOSED OPAMP WITH DYNAMIC POWER OPTIMIZATION

A two-stage operational amplifier (OPAMP) with capability of adjusting the quiescent current dynamically according to the signal condition is proposed in Figure 15. The OPAMP has two separate common-mode feedbacks (CMFBs), one for the first stage and the other for the second stage. The gate bias voltage of the second stage is set by the common-mode voltage of the first stage, which is set by the $M_{o,ref}$ and $I_{o,ref}$. Therefore, $M_{o,ref}$ and M_{op}/M_{om} form a current mirror in the common mode. As a result, the bias current of the second stage is determined as $I_o=I_{o,ref}(W/L)_o/(W/L)_{o,ref}$, which is independent of the first stage current. Although the independent bias current control of the second stage is also possible if the second stage had a tail current source like that in the first stage, it does not have a rail-to-rail output swing due to the voltage headroom of the tail current source. In contrast, the proposed OPAMP has the same characteristics of a typical two-stage OPAMP, including a rail-to-rail output swing.

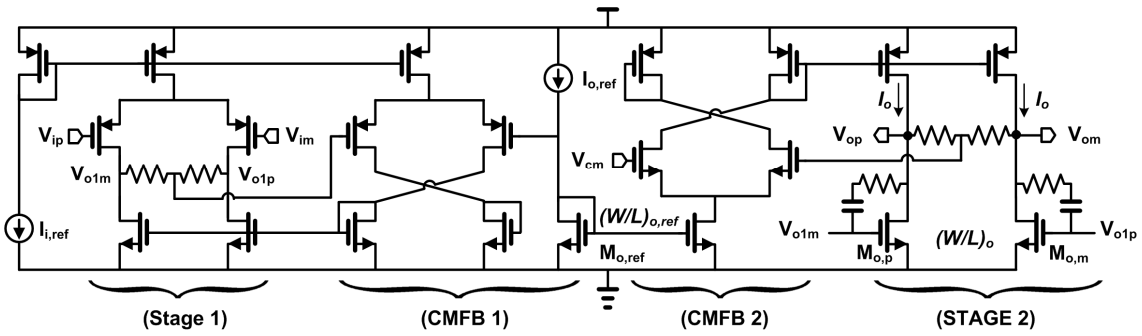

Figure 15. Schematic of proposed OPAMP with quiescent current control.

The proposed topology introduces an additional degree of freedom, which reduces the quiescent current in certain cases. The current of the first stage was determined by the

gain-bandwidth product (GBW) and the input referred noise (IRN) while that of the second stage was determined by the output referred 1-dB compression point (OP1dB). Because small GBWs were sufficient for the low bandwidth, and low OP1dBs were enough for the small signal level, several current reducing scenarios were possible according to the combinations of the requirements of the bandwidth and the signal swing. Although the IRN of the OPAMP increased due to the small current of the first stage in the low bandwidth mode, it did not degrade the overall IRN of the CSF because larger resistors were used in the low-bandwidth mode and the noise contribution of the OPAMPs becomes less dominant. Table 4 summarizes the OPAMP performance at four cases, which are selected as the combinations of the bandwidth and the OP1dB. Only 30 % of the current of the high bandwidth/swing mode was used in the low bandwidth/swing mode.

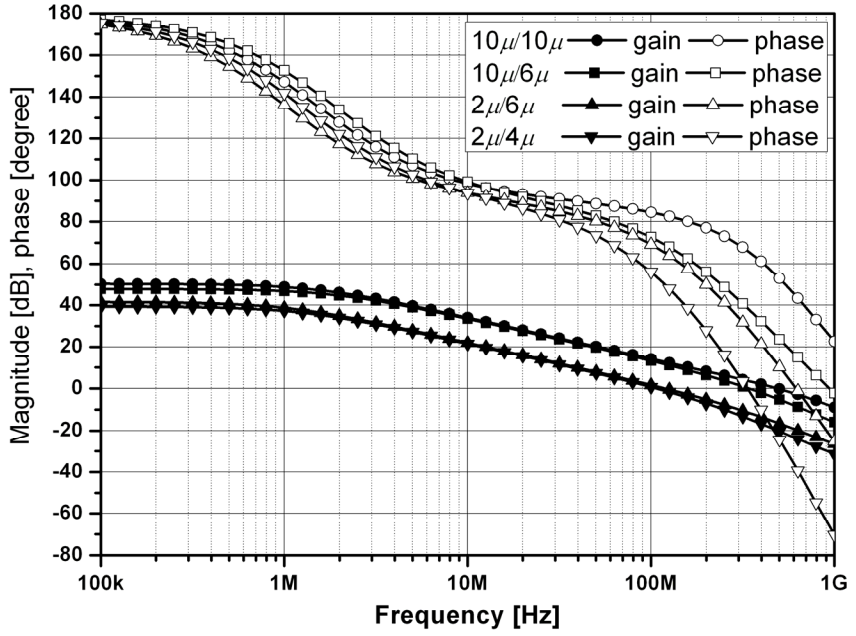

Figure 16. Frequency response of the OPAMP

Table 4. OPAMP performance

Load at each output	kΩ / pF	5 / 0.3		15 / 0.3	
BW / Signal Level		H / H	H / L	L / H	L / L
I_{ref1}/I_{ref2}	μA	10 / 10	10 / 6	2 / 6	2 / 4
DC Gain	dB	44	42	41	39
GBW	MHz	400	360	110	100
Phase Margin	°	61	48	67	55
IRN*	nV / $\sqrt{Hz}$	5	5	7.2	7.2
OP1dB**	dBm	11.4	8.8	14	12
DC Current	μA	400	330	160	120

* Integrated from 1 kHz to 4 MHz.
** 1-MHz single tone is used.

3.5 DC OFFSET COMPENSATION WITH IMPEDANCE BOOSTING

As the maximum gain of the CSF was 30 dB, a DC offset compensation (DCOC) circuit was required to prevent the CSF be saturated from a DC offset. The correction current to eliminate the output DC offset voltage of the CSF was fed to the input of the pre-amplifier as Figure 12(a). The transfer function of the CSF including DCOC block is

$$\frac{A(s)}{1+A(s)\beta(s)} = \frac{A(s)}{1+\dfrac{A(s)}{sC_{oc}\left\{R_{oc2}\left(1+k\right)+R_{oc1}\right\}}}, \tag{3}$$

where $A(s)$ and $\beta(s)$ stand for transfer functions of the CSF and the DCOC block, respectively. To reduce the silicon area, the effective time constant of the DCOC block was boosted by T-network consists of R_{oc1}, R_{oc2}, and R_{oc3} as a factor of $(1+k)$ [4].

However, the offset voltage of an OPAMP in the DCOC block, OP_{oc}, appeared at the output of the CSF with the same amplification factor of $(1+k)$, so it could not be arbitrarily large. A simulation result of the low-cutoff bandwidth and the output DC offset voltage verifies the dependency on $(1+k)$ in Figure 17. In this design, $(1+k)$ was assigned to three to meet to the maximum sustainable input offset voltage of the following PGA. In addition, as the low-cutoff bandwidth of the CSF was proportional to the gain of the CSF as $A(s)/2\pi C_{oc}\{R_{oc2}(1+k)+R_{oc1}\}$, the low-cutoff bandwidth would be varied due to the CSF gain change. It was solved by adjusting R_{oc2} according the gain change.

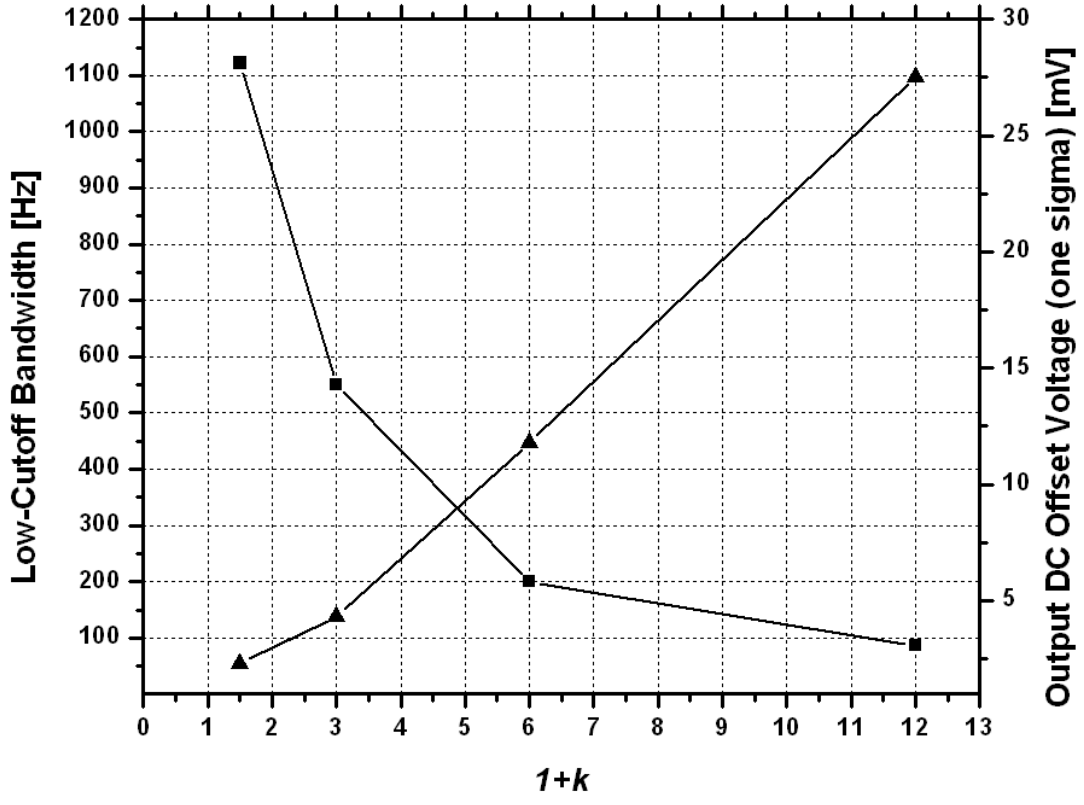

Figure 17. Low-cutoff bandwidth and output DC offset voltage versus (1+k).

3.6 BANDWIDTH CALIBRATION

Figure 12(c) shows a simplified schematic of an automatic calibration block for the bandwidth adjustment. Because RC products determined the coefficients of the CSF, as Equation 1, the calibration block found a proper RC product for the required bandwidth.

Replicas of the BIRB and the capacitor bank of the signal path were used in the calibration block. Three reference voltages, V_{refc}, V_{refp}, and V_{refm} were generated from internal band-gap reference circuitry, and a current, $(V_{refp}-V_{refm})/R_{cal}$, was integrated with the C_{cal} during integrating period (ϕ_2). Then, the comparator examined the integrated voltage with respect to $V_{refp}-V_{refm}$ as ϕ_1 and ϕ_2 became high and low, respectively. Because the integrating period, ϕ_2, was precisely determined by an external reference clock, the proper RC code was obtained as

$$\frac{V_{refp}-V_{refm}}{R_{cal}C_{cal}}T_{\phi 2}=V_{refp}-V_{refm}. \tag{4}$$

3.7 IMPLEMENTATION AND MEASUREMENT RESULT

The proposed CSF was fabricated as a building block of a mobile-TV receiver using a 0.18-μm CMOS 1P5M process, as shown in Figure 18. The performance of the CSF was evaluated after it was packaged in a leadless plastic package. The measured spectrum at the output of the CSF is shown in Figure 19. Figure 20 shows the frequency response with several combinations of the codes for the BIRBs and the capacitor banks. The CSF covered 0.5–6 MHz, which supports the required bandwidth of 0.75–4 MHz

for DVB-H/T and T-DMB/DAB with sufficient margins for the PVT variations from the resistance variation of ±21% and the capacitor deviation of ±15%. Figure 21 shows the capability of the gain control of the CSF in the 4-MHz bandwidth mode. The gain control range was 30dB, and the step was 6dB. However, the noise and the IIP_3 of only the CSF could not be measured because the CSF was used as a block of the receiver. Therefore, simulated values were used for the noise and the IIP_3 performance for the comparison purpose.

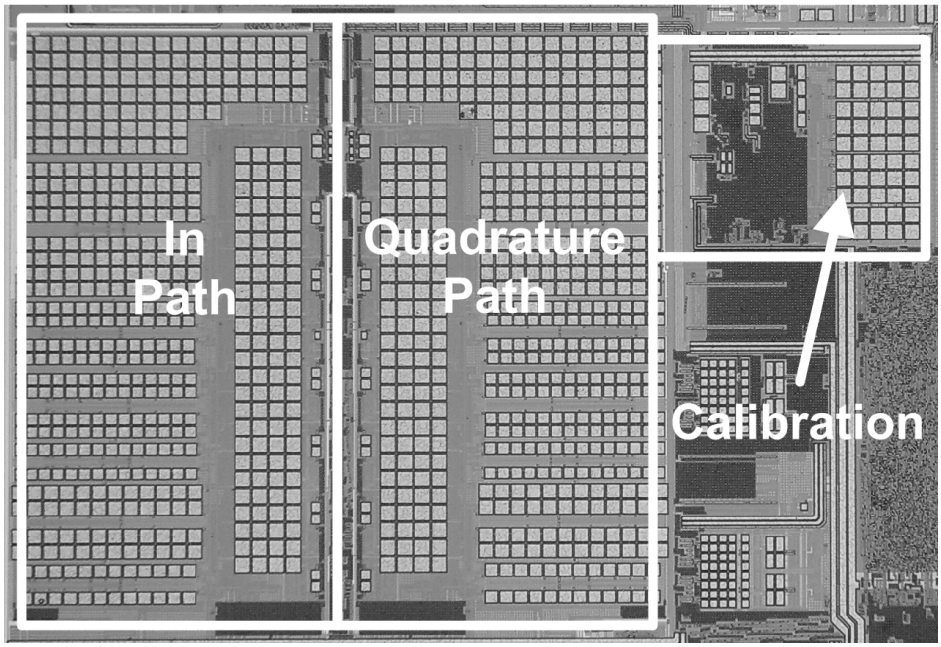

Figure 18. Microphotograph of the CSF.

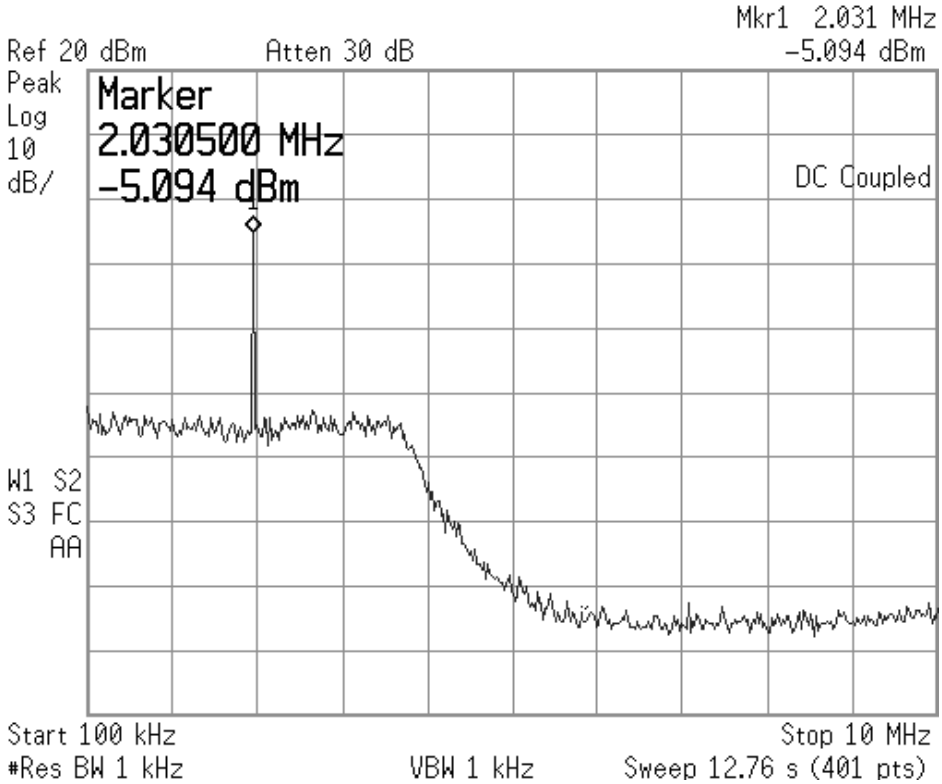

Figure 19. Measured spectrum of the CSF output

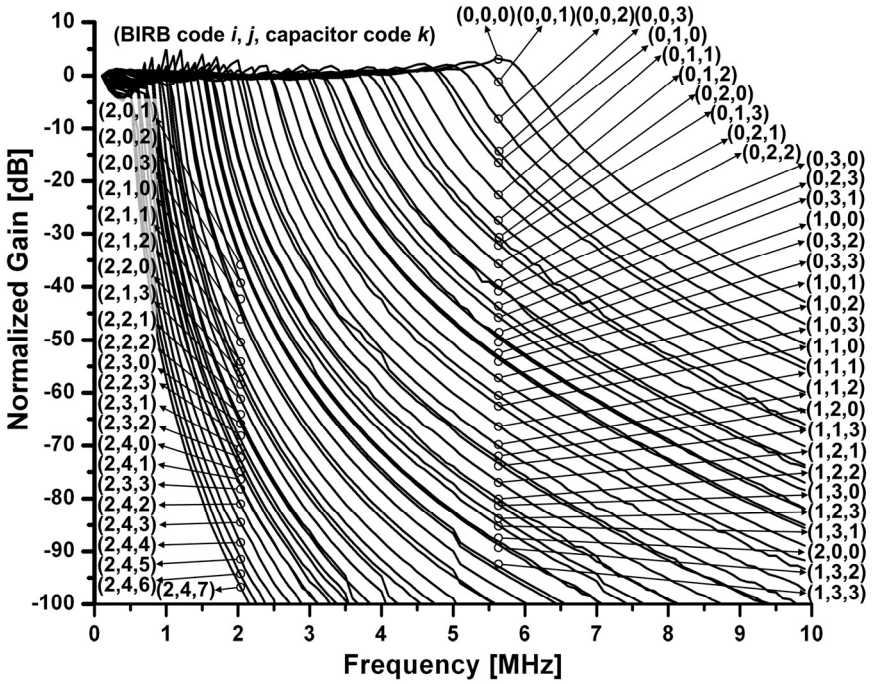

Figure 20. Frequency response of the CSF.

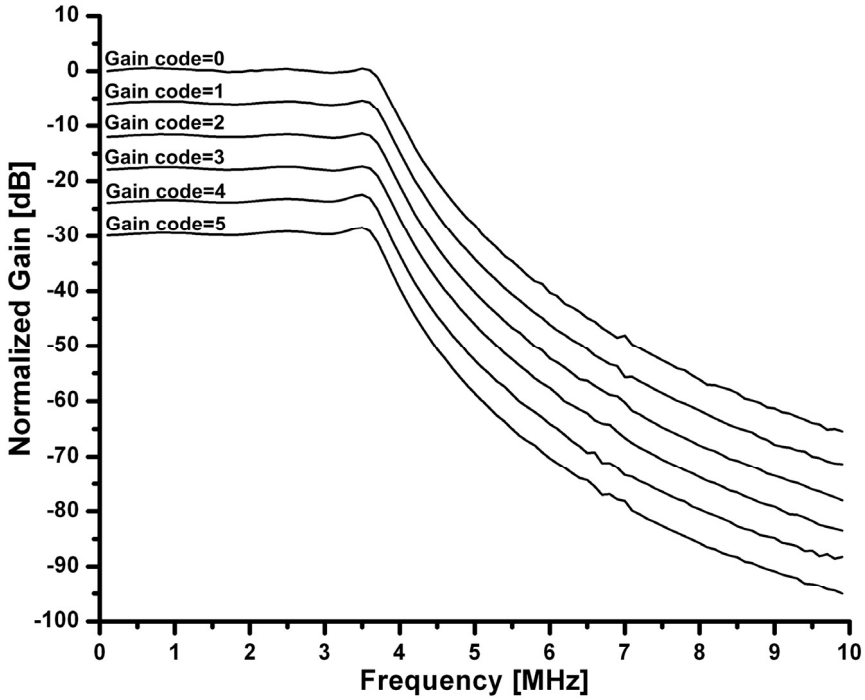

Figure 21. Gain control when the bandwidth was 4MHz.

3.8 COMPARISON TO PREVIOUS WORKS

The performance of this work is compared with that of previously published CSFs in Table 5, which shows that the former is superior to the latter with respect to the wide pseudo-continuous bandwidth-tuning range and the wide gain control range with fine steps.

Table 5. Comparison to previous works.

	Unit	[3]	[4]#	[5]##	This work
Technology	μm	0.13	0.12	0.18	0.18
Supply	V	1.0	1.0	1.2	1.8
Topology*		C/I	C/E	C	C
Order		1/3/5	5	5	6
Bandwidth Range	MHz	1-20	5 / 10	0.1	0.5 - 6
Bandwidth Step	%	Cont.	5	No	5
Gain Range	dB	No	No	48	30
Gain Step	dB	No	No	24	6
Input Referred Noise (High / Low BW)	$nV/\sqrt{Hz}$	85-52	140/143	607-19.3	15-29
Power Consumption	mW	3.0-7.5	6.1/6.1	0.46-2.67	3.4-5.0
Active Area**	mm^2	1.94	0.17	1.2	0.64

* C: Chebyshev-I, I: Inverse Chebyshev, E: Elliptic.

** A single path without calibration circuitry for the comparison.

Only in-band IIP_3 performance is reported.

Low-power / high-power mode instead of high-BW / low-BW mode.

3.9 CONCLUSIONS

In this chapter, an active-RC low-pass filter with binary interpolated resistor banks (BIRB) has been proposed to achieve a wide pseudo-continuous bandwidth-tuning range and fine gain steps for supporting multiple standards with the optimized signal levels and relaxing requirements of a succeeding PGA block. By the coarse bandwidth tuning using the proposed BIRB and minimizing the capacitor resolution, the silicon area was reduced. The filter achieved over a one-decade bandwidth tuning range with 5% steps and a 30-dB dynamic range with 6-dB steps.

CHAPTER 4

RF FRONT-END WITH INTERFERER-CANCELLATION

4.1 INTRODUCTION

In this chapter, a multi-band RF front-end with the interference-cancellation capability is presented. First, the required amount of the TX cancellation is derived from the WCDMA standard. Then, a method to achieve robust cancellation on the PVT and external component variations is presented. The detailed description on the block level design is also presented. Finally, the effectiveness of the proposed method is demonstrated by the measurement result.

4.2 SPECIFICATIONS FOR INTERFERENCE-CANCELLATION RECEIVER

In this section, WCDMA receiver RF specifications are derived from the WCDMA standard. From the derived RF specifications, the requirements of a LNA, a mixer, and a TX leakage canceller are investigated.

Among the required performance of user equipment of the WCDMA standard specified in [1], the receiver RF specifications are summarized in Table 6.

Table 6. WCDMA RF receiver specifications in band-I and power class 3 [1].

Test Conditions	**Unit**	**Specification**
Common parameters		
TX frequency	MHz	1920-1980
RX frequency	MHz	2110-2170
Signal bandwidth	MHz	3.84
Maximum TX power	dBm	25
Reference sensitivity test		
Received power	dBm/3.84MHz	-106.7
Adjacent-channel selectivity test		
Received power	dBm/3.84MHz	-92.7
Modulated interferer at ±5 MHz offset	dBm/3.84MHz	-52
In-band blocking test		
Received power	dBm/3.84MHz	-103.7
Modulated interferer at ±10 MHz offset	dBm/3.84MHz	-56
Modulated interferer at ±15 MHz offset	dBm/3.84MHz	-44
Out-of-band blocking test		
Received power	dBm/3.84MHz	-103.7
CW interferer at 2050-2095 or 2185-2230 MHz	dBm	-44
CW interferer at 2025-2050 or 2230-2255 MHz	dBm	-30
CW interferer at 1-2025 or 2255-12750 MHz	dBm	-15
Inter-modulation test		
Received power	dBm/3.84MHz	-103.7
CW interferer at ±10 MHz offset	dBm	-46
Modulated interferer at ±20 MHz offset	dBm/3.84MHz	-46

As a duplexer isolates a weak RX signal from a strong TX signal, it plays an important role in the WCDMA RF system. The summary of a typical FBAR duplexer is listed in Table 7 [7]. With assumption of the TX front-end insertion loss (TX_FEIL) plus

TX insertion loss (TXIL) of the duplexer of 3 dB, the maximum output power at the output of a power amplifier (PA) is 28 dBm. Therefore, the TX leakage at the LNA input is *28dBm – 53dB = -25dBm* ($P_{TX,LEAK}$).

Table 7. Typical WCDMA duplexer performance [7].

	Unit	Specification
TX band insertion loss (TXIL)	dB	1.6
RX band insertion loss (RXIL)	dB	2.0
TX-RX isolation in TX band	dB	53
TX-RX isolation in RX band	dB	43
RX band insertion loss at 380MHz (double duplex) offset	dB	45

4.2.1 Sensitivity

The required carrier-to-noise ratio (CNR) for the bit-error rate (BER) 0.001 is -7.6 dB [15]. To account for the implementation margin from the imperfection of the received signal and phase error, the minimum required (CNR_{min}) is assigned to -6.6 dB. Because -106.7 dBm is received for the reference sensitivity test, the total noise power referred at the antenna input needs to be less than -100.1 dBm. As the RX front-end insertion loss (RX_FEIL) plus the RX insertion loss (RXIL) of the duplexer can be up to 4 dB, the maximum noise and distortion power ($P_{ND,total}$) referred at the receiver input is -104.1 dBm. Since thermal noise over 3.84-MHz bandwidth (P_{th}) is -108.1 dBm, the maximum noise figure (NF_{max}) is

$$NF_{\max} = -107.6dBm - P_{th} - CNR_{\min} - RX\_FEIL - RXIL = 4dB. \quad (5)$$

Although the 4-dB NF is enough to meet the sensitivity requirement, 3-dB NF is assumed in this thesis to achieve better sensitivity performance.

4.2.2 Out-of-band IIP_2 and IIP_3 specifications for out-of-band blocker test

Since the input-referred second-order intercept point (IIP_2) and the third-order intercept point (IIP_3) determines distortion power from interferers, they are critical parameters for a direct-conversion receiver as shown in Figure 6. The IIP_2 and the IIP_3 can be classified as in-band $IIP_{2,IB}$ and $IIP_{3,IB}$; or out-of-band $IIP_{2,OB}$ and $IIP_{3,OB}$ according to the existence of attenuation of the interferers between an LNA and a mixer. In determining the $IIP_{2,OB}$ and $IIP_{3,OB}$ specifications, the worst case scenario is when an out-of-band interferer lies at the double duplex frequency—380 MHz. As shown in Table 6 and 7, the power of the interferer is -15 dBm at the antenna and the duplexer attenuation at the double duplex offset is 45 dB in the worst case. Therefore, the power of the interferer at the LNA input (P_{INT}) is $-15dBm - 45dB - 2dB\ (RX\_FEIL) = -62dBm$.

To achieve CNR_{min}, $P_{ND,Total}$ needs to be less than $-103.7dBm + 6.6dB = -97.1dBm$. $P_{ND,Total}$ is composed of the total thermal noise with the receiver NF ($P_{th,RX}$), the second-order distortion from the TX leakage ($P_{IMD2,OB}$), and the third-order distortion from the interferer and the TX leakage ($P_{IMD3,OB}$). Other noises such as the RX band noise from the PA, the reciprocal mixing of the phase noise of the LO signal with the TX leakage and the interferer, and the cross modulation between the TX leakage and the interferer are all negligible. First, $P_{th,RX}$ is -105 dBm as $P_{th} + NF = -105dBm$. $P_{IMD2,OB}$ is expressed as Equation 6 [18]

$$P_{IMD2,OB} = 2(P_{TX,LEAK} - 3) - IIP_{2,OB} \quad (6)$$

, where the modulated TX leakage is modeled as two sinusoidal tones. Finally, $P_{IMD3,OB}$ is represented by Equation 7 [18]

$$P_{IMD3,OB} = 2P_{TX,LEAK} + P_{INT} - 2IIP_{3,OB}. \quad (7)$$

Therefore, $P_{ND,Total}$ is calculated as Equation 8

$$P_{ND,Total} \approx P_{th,RX} + P_{IMD2,OB} + P_{IMD3,OB} = 10\log\left(10^{\frac{-105}{10}} + 10^{\frac{-56-IIP_{2,OB}}{10}} + 10^{\frac{-50+P_{INT}-2IIP_{3,OB}}{10}}\right) \le -97.1dBm. \quad (8)$$

Figure 22 shows the $P_{ND,Total}$ versus the $IIP_{2,OB}$ and the $IIP_{3,OB}$ with a 3-dB stronger out-of-band interferer than the WCDMA standard minimum specification. In conclusion, the $IIP_{2,OB}$ and the $IIP_{3,OB}$ should be better than 50 dBm and -5 dBm, respectively.

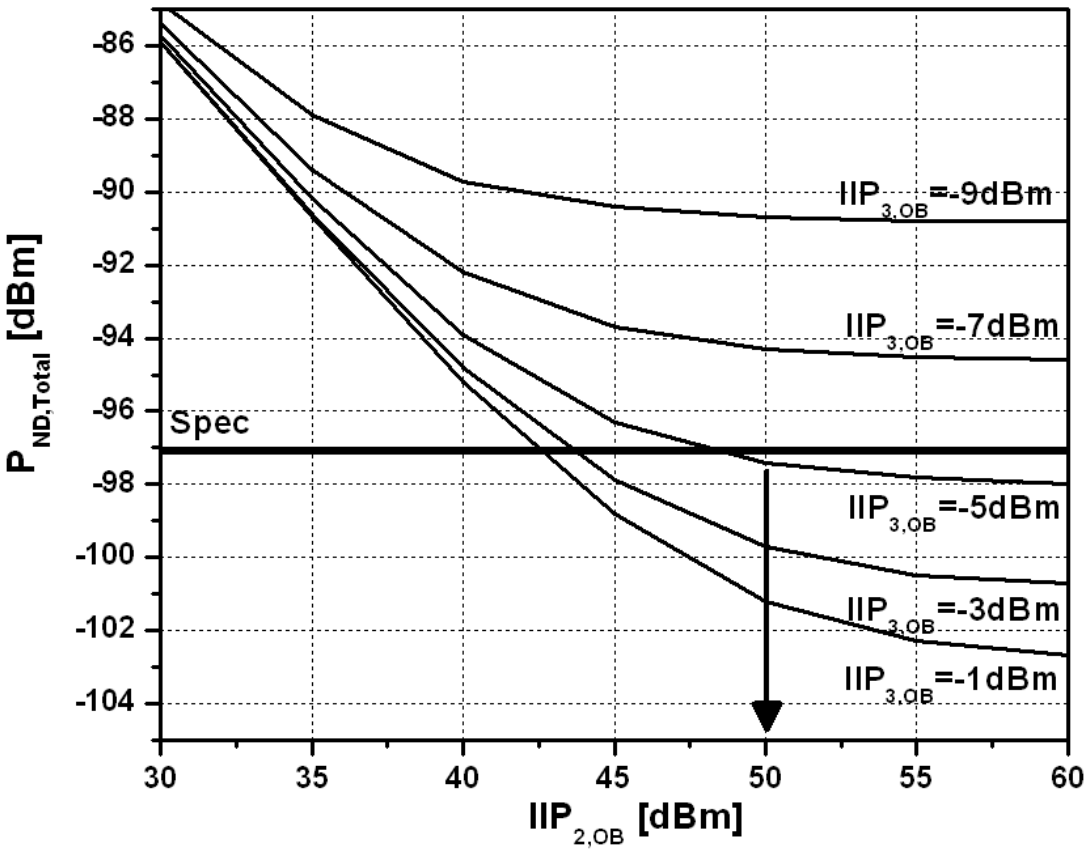

Figure 22. $P_{ND,Total}$ versus $IIP_{2,OB}$ and $IIP_{3,OB}$.

4.2.3 In-band IIP_3 specification for inter-modulation test

The in-band $IIP_{3,IB}$ specification is determined by the inter-modulation test. Unlike the out-of-band blocking test whose out-of-band interferers are attenuated by SAW filters, the inter-modulation interferers are not attenuated by the SAW filters. Therefore, the $IIP_{3,IB}$ of the mixer dominates the $IIP_{3,IB}$ of the overall receiver. Similar to Equation 7, the distortion power ($P_{IMD3,IB}$) from the inter-modulation interferers (P_{INT}) is derived by Equation 9

$$P_{IMD3,IB} = 3(P_{INT} - RX\_FEIL - RXIL) - 2IIP_{3,IB}. \quad (9)$$

Similar to Equation 8, $P_{ND,Total}$ is calculated as Equation 10

$$P_{ND,Total} \approx P_{th,RX} + P_{IMD2,OB} + P_{IMD3,IB} = 10\log\left(10^{\frac{-105}{10}} + 10^{\frac{-56-IIP_{2,OB}}{10}} + 10^{\frac{3(P_{INT}-4)-2IIP_{3,IB}}{10}}\right) \le -97.1dBm. \quad (10)$$

Provided that $IIP_{2,OB}$ is 50 dBm, the required in-band $IIP_{3,IB}$ for interferer that are 3-dB stronger than the WCDMA standard minimum is -21 dBm.

4.2.4 In-band IIP_2 specification for in-band blocking test

Similar to the $IIP_{3,IB}$ specification determined by the inter-modulation test, the in-band $IIP_{2,IB}$ specification is determined by the in-band blocking test. As a -44dBm interferer at ±15-MHz offset frequency is the worst condition, the second-order distortion power ($P_{IMD2,IB}$) is calculated by Equation 11

$$P_{IMD2,IB} = 2(P_{BLK} - RX\_FEIL - RXIL - 3) - IIP_{2,IB} \quad (11)$$

, where the WCDMA modulated signal is model as two sinusoidal tones same as Equation 6. Similar to Equation 8, $P_{ND,Total}$ is calculated by Equation 12

$$P_{ND,Total} \approx P_{th,RX} + P_{IMD2,OB} + P_{IMD3,IB} = 10\log\left(10^{\frac{-105}{10}} + 10^{\frac{-56-IIP_{2,OB}}{10}} + 10^{\frac{2(P_{BLK}-3)-IIP_{2,IB}}{10}}\right) \le -97.1dBm. \quad (12)$$

Provided that $IIP_{2,OB}$ is 50 dBm, the required $IIP_{2,IB}$ with an interferer that is 3-dB stronger than the WCDMA standard minimum is 3 dBm. Table 8 provides the summary of the receiver specifications.

Table 8. WCDMA receiver specifications.

	Unit	Specification	Main source
NF	dB	3	Thermal noise
$IIP_{2,IB}$	dBm	3	In-band blocker
$IIP_{2,OB}$	dBm	50	TX leakage
$IIP_{3,IB}$	dBm	-21	Inter-modulation
$IIP_{3,OB}$	dBm	-5	TX and double duplex

4.2.5 LNA and down-conversion mixer specifications

The specifications of the LNA and the mixer can be derived from Table 8. With an inter-stage filter having insertion loss (IL) and out-of-band attenuation (A_{OB}), the total NF, IIP_3, and IIP_2 are derived as Equation (13)-(17) [18]

$$NF_{Total} = 10\log 10\left(F_{LNA} + \frac{F_{mixer} - 1}{G_{LNA} - IL}\right) \quad (13)$$

$$IIP_{2,IB} = IIP_{2,mixer} + IL - G_{LNA} \tag{14}$$

$$IIP_{2,OB} = IIP_{2,mixer} + IL - G_{LNA} + 2A_{OB} \tag{15}$$

$$\frac{1}{IIP_{3,IB,linear}} = \frac{1}{IIP_{3,LNA,linear}} + \frac{G_{LNA,linear} / IL_{linear}}{IIP_{3,mixer,linear}} \tag{16}$$

$$\frac{1}{IIP_{3,OB,linear}} = \frac{1}{IIP_{3,LNA,linear}} + \frac{G_{LNA,linear} / IL_{linear}}{IIP_{3,mixer,linear}} \frac{1}{10^{3A_{OB}/40}} \tag{17}$$

, where $IIP_{3,linear}$, $G_{LNA,linear}$, and IL_{linear} stand for the linear-scale values of the IIP_3, the LNA gain, and the insertion loss, respectively. Interesting advantages of adopting filter are the last terms of Equation 15 and 17: Because of the A_{OB}, the $IIP_{2,OB}$ and the $IIP_{3,OB}$ are boosted the amounts of $2\times A_{OB}$ and $1.5\times A_{OB}$—these are the main reasons of adopting SAW filters. However, if only TX leakage is attenuated and other interferers remain same, Equation 17 changes to Equation 18

$$\frac{1}{IIP_{3,OB,linear}} = \frac{1}{IIP_{3,LNA,linear}} + \frac{G_{LNA,linear} / IL_{linear}}{IIP_{3,mixer,linear}} \frac{1}{10^{2A_{TX}/40}}. \tag{18}$$

, where A_{TX} is the amount of TX leakage attenuation. The required IIP_3 and IIP_2 of the LNA and the mixer to meet the specifications for various amounts of TX leakage cancellation are shown in Figure 23 and summarized in Table 9(b). As shown in Figure 22, the linearity requirement of the mixer is fairly relaxed as the TX cancellation

increasing. In Table 9, because a DC blocking capacitor is used after a LNA, the IIP_2 of the LNA is meaningless. As the mixer does not have frequency selectivity, the worst values between $IIP_{2,OB}$ and $IIP_{2,IB}$; and $IIP_{3,OB}$ and $IIP_{3,IB}$ becomes the specifications of the IIP_2 and the IIP_3. For the TX cancellation of 20 dB, the mixer should have the 4-dBm IIP_3 and the 25-dBm IIP_2 those are easily achievable.

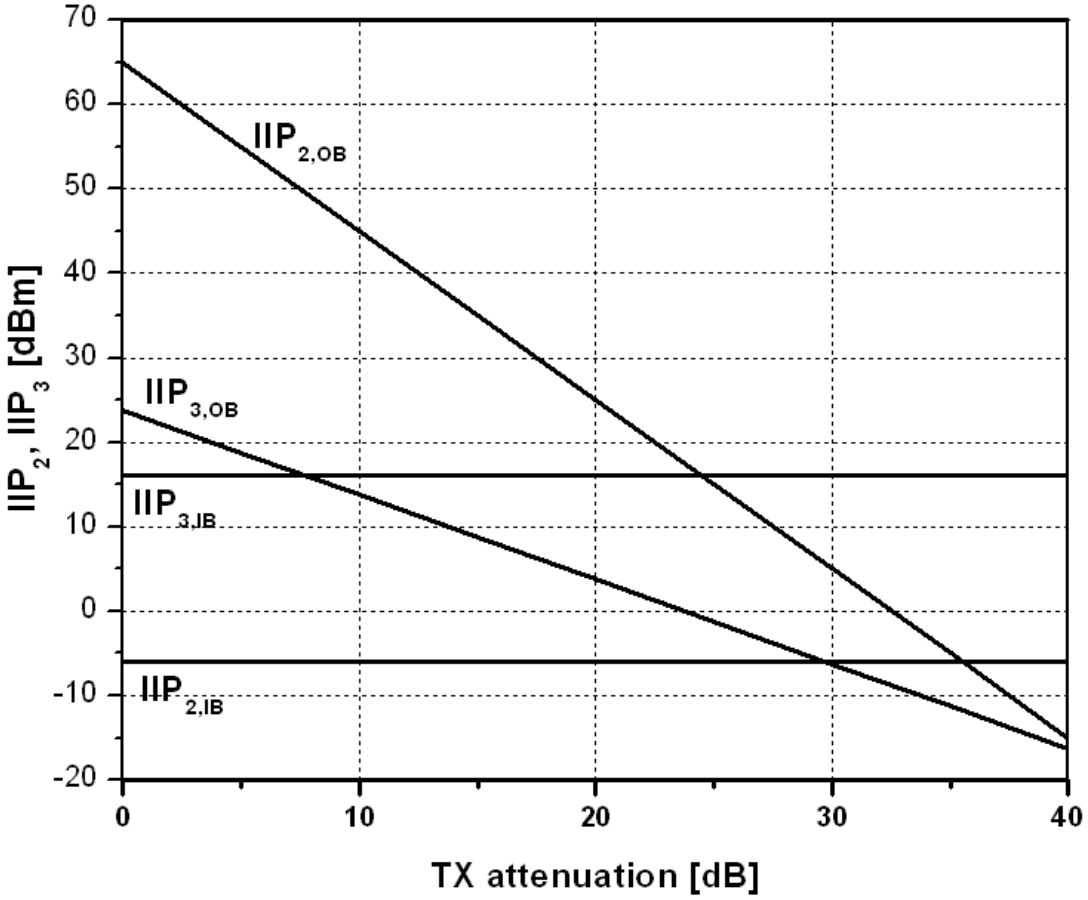

Figure 23. Required IIP_2 and IIP_3 of mixer versus TX cancellation.

Table 9. LNA and mixer specifications with SAW and 20-dB TX attenuation.

(a) With commercial SAW filter (insertion loss=2 dB) [9]				
	Unit	LNA	Mixer	Total
Gain	dB	15	20	33
NF	dB	1.5	10	2.75
$IIP_{2,IB}$	dBm	-	16	3
$IIP_{2,OB}$	dBm	-	-1	50
$IIP_{3,IB}$	dBm	-3	-8	-3
$IIP_{3,OB}$	dBm	-3	-26	-5
(b) With 20-dB TX attenuation (NF=0.5 dB)				
	Unit	LNA	Mixer	Total(IB/OB)
Gain	dB	15	20	35
NF	dB	1.5	10	2.72
IIP_2	dBm	-	25	10/50
IIP_3	dBm	-3	4	-12/-5

4.3 Design Principle for Multi-Band Interference-Cancellation Receiver

In this section, a technique to realize the TX leakage cancellation is presented for multi-band applications. Although research has been investigated to realize SAW-less receivers as described in Chapter 2, each technique has its drawback [10]-[12]. A method to achieve robust cancellation on the PVT and external component variations are presented. In addition, an approach to operate the canceller in multi-band will be addressed.

4.3.1 Frequency conversion feedback

Because the TX frequency is only 190-MHz lower than the RX frequency of 2000 MHz, it is not feasible to attenuate the TX leakage in the RF frequency. The quality factor of LC resonators in silicon-based integrated circuits is too low to attenuate the TX leakage without considerable loss in the RX frequency. To solve this problem, a frequency translation technique was reported and it has been utilized for a feedback loop to cancel the TX leakage signal [12]. However, the previous approach has following problems: Because the feedback loop was connected at the junction of the LNA input and a duplexer RX port, the undetermined impedance of the duplexer RX port at TX frequency made the feedback loop unpredictable. Figure 24 (a) and (b) shows the return loss and the location of the reflection coefficient of a typical duplexer RX port at the TX frequency, respectively [7]. Although the impedance of the RX port is 50 ohm at the RX frequency, it is not 50 ohm outside at the TX frequency. Since the reflection coefficient rotates around the Smith chart as the measurement point apart from the duplexer in the TX frequency, the impedance of the RX port at the TX frequency varies from short to open according to the distance between the duplexer and the receiver. Therefore, the feedback loop characteristics used in the reference [12] are unpredictable.

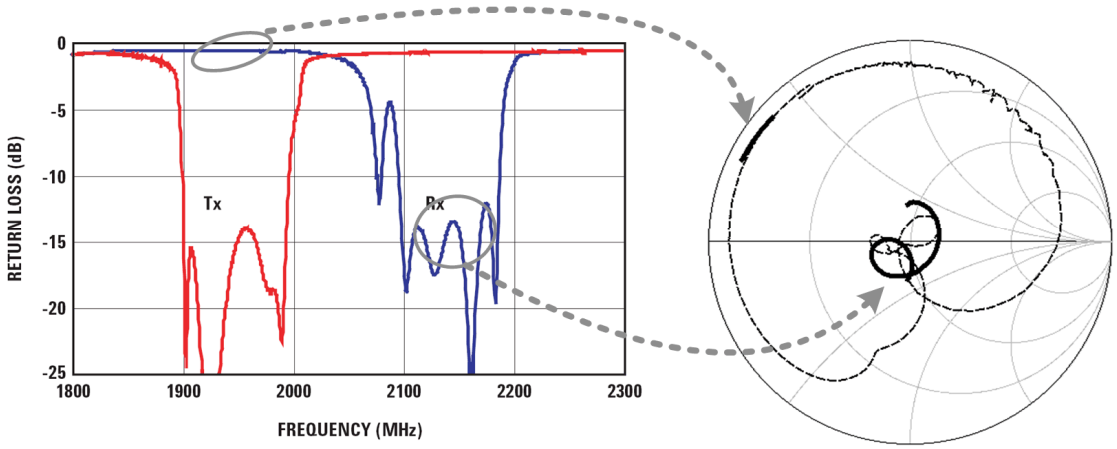

(a) (b)

Figure 24. Duplexer RX port (a) return loss, (b) reflection coefficient.

A new technique to connect the feedback loop to the LNA load inductor is proposed in the dissertation as shown in Figure 25. First, the RX signal part is designed as follows. To reduce pin counts and external components, as compared to the previous approach [12], the LNA has a single-ended input. The LNA is consists of a common-source trans-conductance stage followed by a common-gate cascade stage, which improves the RX LO leakage to the LNA input, and a tuned load with an inductor and capacitors. Then, RX passive mixers convert the RX signal to DC. Passive mixers are used to improve the linearity of the mixer [19].

Another part of this method is TX leakage cancellation part. By adopting TX LO signals which already exists in TX blocks, the TX leakage at the LNA output is down-converted to DC by first passive mixers. The down-converted RX signal which lies at the duplexer frequency is attenuated by LPFs realized with TIAs, but the TX leakage around DC is not attenuated by the LPFs. Then, the TX signal at DC is up-converted to the original TX frequency by up-conversion mixers. Finally, the TX signal is fed to the LNA

load and cancels the TX signal from the LNA. By attenuating the RX signal in the feedback loop, the loop gain of the RX signal becomes small not to affect the RX signal. The operating principle is illustrated in Figure 26. To support multi-band with a single TX canceller, the TX LOs for the down-conversion mixer are fed from a phase rotator, which will be discussed in the next section in detail.

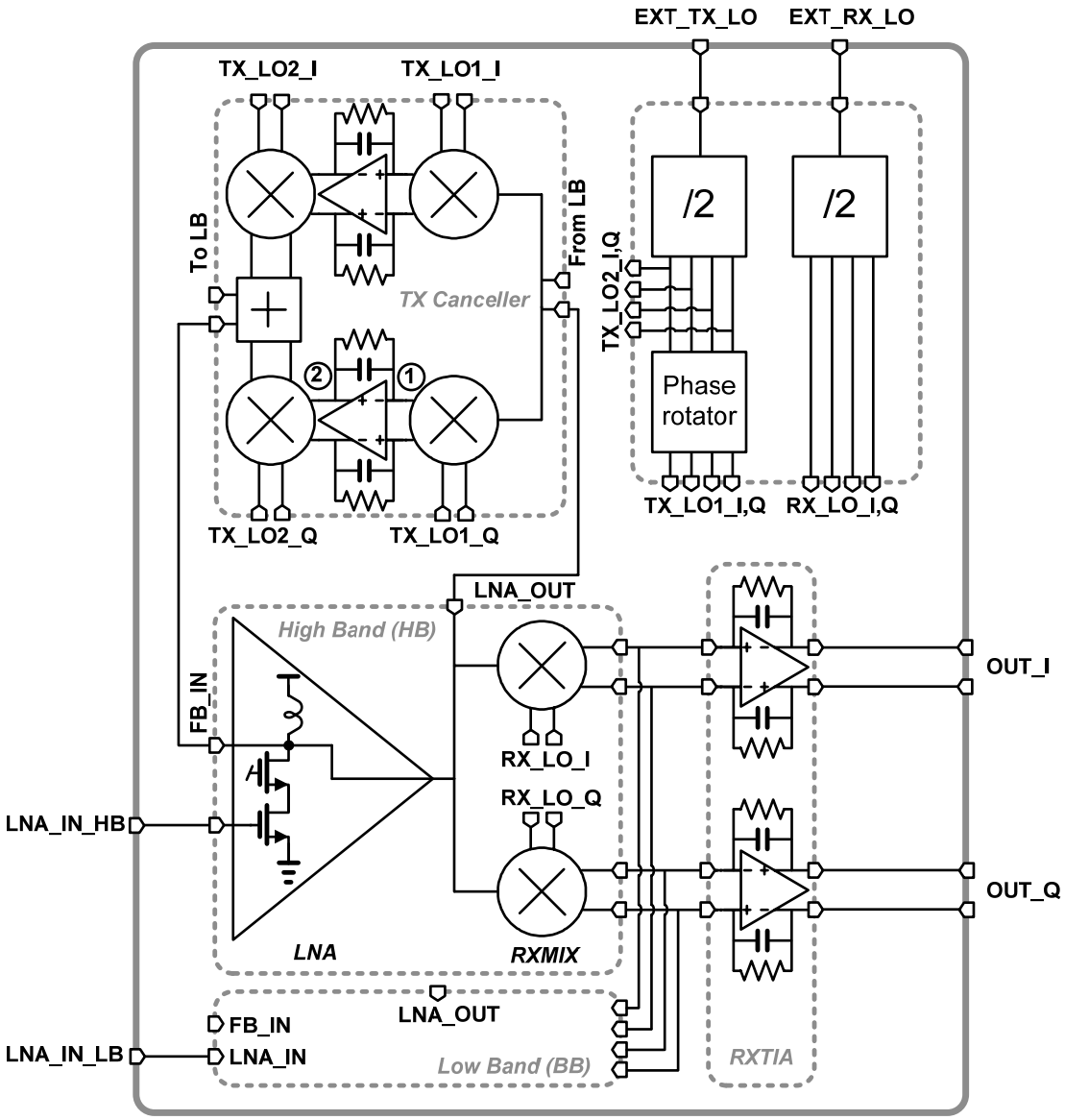

Figure 25. Proposed TX cancellation RF front-end.

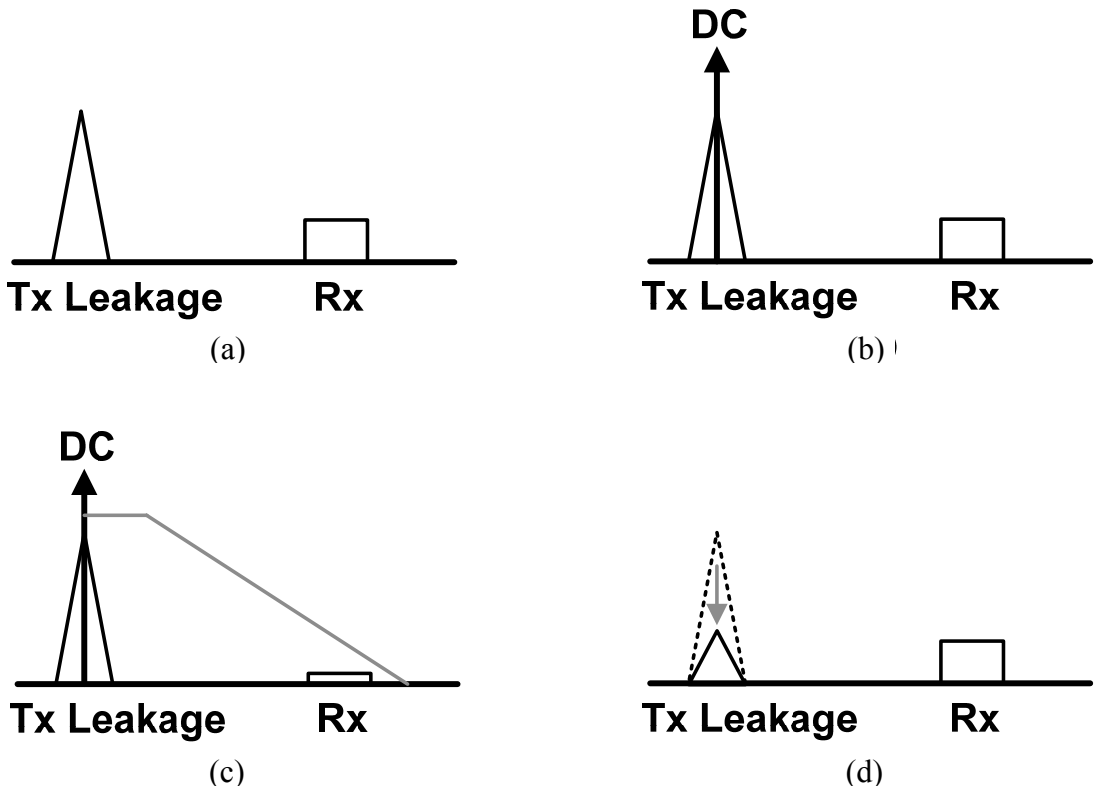

Figure 26. Principle of proposed TX leakage cancellation (a) LNA input, (b) output of down-conversion mixer in TX canceller (①), (c) output of TIA in TX canceller (②), (d) LNA output.

4.3.2 Phase adjustment for multi-band applications

The feedback loop experiences phase shifts around the loop by several blocks such as the down-converter, the up-converter, and the LNA load. Because these phase shifts originate from the parasitic capacitors in the RF frequency, they are changeable according to the RF frequency. If $\tau 1$, $\tau 2$, and $\tau 3$ stand for the time delays of the LNA, the first down-conversion mixer of the TX canceller, and the second up-conversion mixer of the TX canceller, respectively, the phase shift due to these time delay is

$f_{tx}(\tau 1+\tau 2+\tau 3)\times 360°$. Therefore, for multi-band applications, the phase shift around the feedback loop needs to be adjusted to guarantee the stability of the loop.

To adjust phase of the loop, the phase response of the TX canceller output according to the TX_LO1 and TX_LO2 are investigated. If the input of the TX canceller, TX_LO1, and TX_LO2 are presented as $cos(\omega_{in}t)$, $cos(\omega_{LO}t+\phi)$, and $cost(\omega_{LO}t+\theta)$, respectively, the output of the TX canceller is calculated to $\cos(\omega_{in}t+\phi-\theta)$ with normalization in the amplitude. Therefore, to change the phase of the TX canceller output—$\phi-\theta$, the phase of TX_LO1 or TX_LO2 should be adjusted independently. To rotate the phase of TX_LO1 with respect to TX_LO2, a phase shifter is designed as Figure 27 [20]. Adding two quadrature signals with adjustable strength, α can then change the LO phase as Equation 19. To attenuate noise from the phase rotator by the LPF, the rotated LO signals are connected to the down-converters.

$$TX\_LO1\_I=\alpha\cos\left(\omega_{LO}t\right)+\left(1-\alpha\right)\sin\left(\omega_{LO}t\right)=\sqrt{2\alpha^2-2\alpha+1}\cos\left(\omega_{LO}t-\tan^{-1}\frac{1-\alpha}{\alpha}\right)$$

$$TX\_LO1\_Q=\left(1-\alpha\right)\cos\left(\omega_{LO}t\right)+\alpha\sin\left(\omega_{LO}t\right)=\sqrt{2\alpha^2-2\alpha+1}\sin\left(\omega_{LO}t-\tan^{-1}\frac{1-\alpha}{\alpha}\right). \quad (19)$$

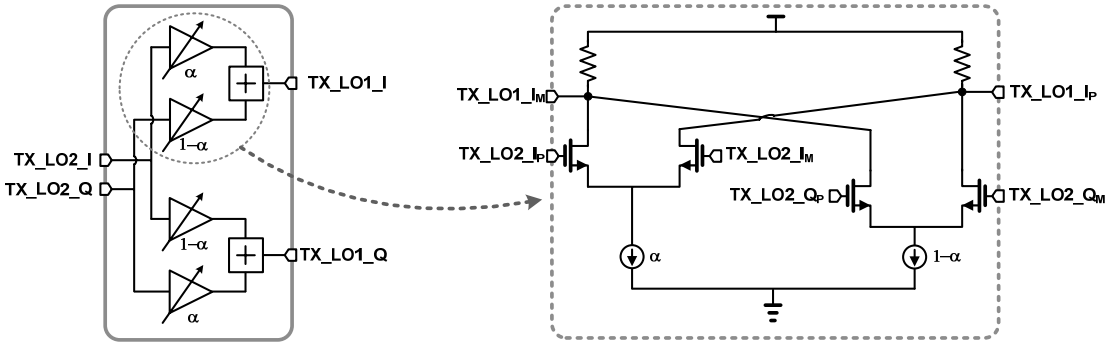

Figure 27. LO phase rotator.

4.3.3 Block level design

In this section, the design of the signal part and the TX canceller part is presented.

4.3.3.1 Signal part

The schematic of the signal part in the transistor level for one frequency band is shown as Figure 28. As shown in Figure 25, the low band and the high band have separate LNAs and mixers but they share the TIA. The LNA is a simple common-source cascode structure [21], [22]. A passive mixer followed by TIAs is used for the down-conversion mixer as it consumes lower power while achieving higher linearity than an active mixer. Research has been performed to overcome the high noise problem of the passive mixer [23]-[25]. For the OPAMP in the TIA, the dual common-mode feedback structure presented in Chapter 3 is used to reduce the quiescent current.

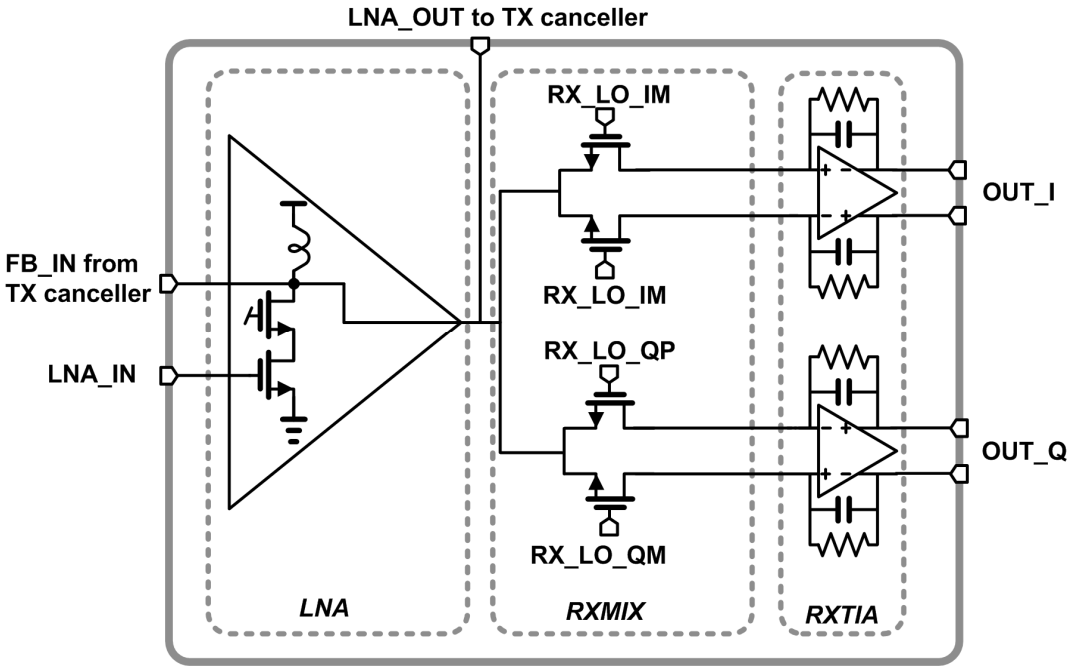

Figure 28. Schematic of the signal path.

4.3.3.2 Low-noise amplifier

A low-noise amplifier (LNA) is used to reduce the noise contribution of the following mixer as shown in Figure 29. As the TX cancellation occurs at the output of the LNA, the linearity of the LNA needs to be high. A linearization method of the post-distortion is adopted in this design [22]. The adjusting the bias point of the auxiliary MOSFET, M_{aux}, it eliminates the 3rd-order non-linearity of the main MOSFET. To set the bias points of the main MOSFET and the auxiliary MOSFET, two current mirrors, M_{main_bias} and M_{aux_bias}, are used.

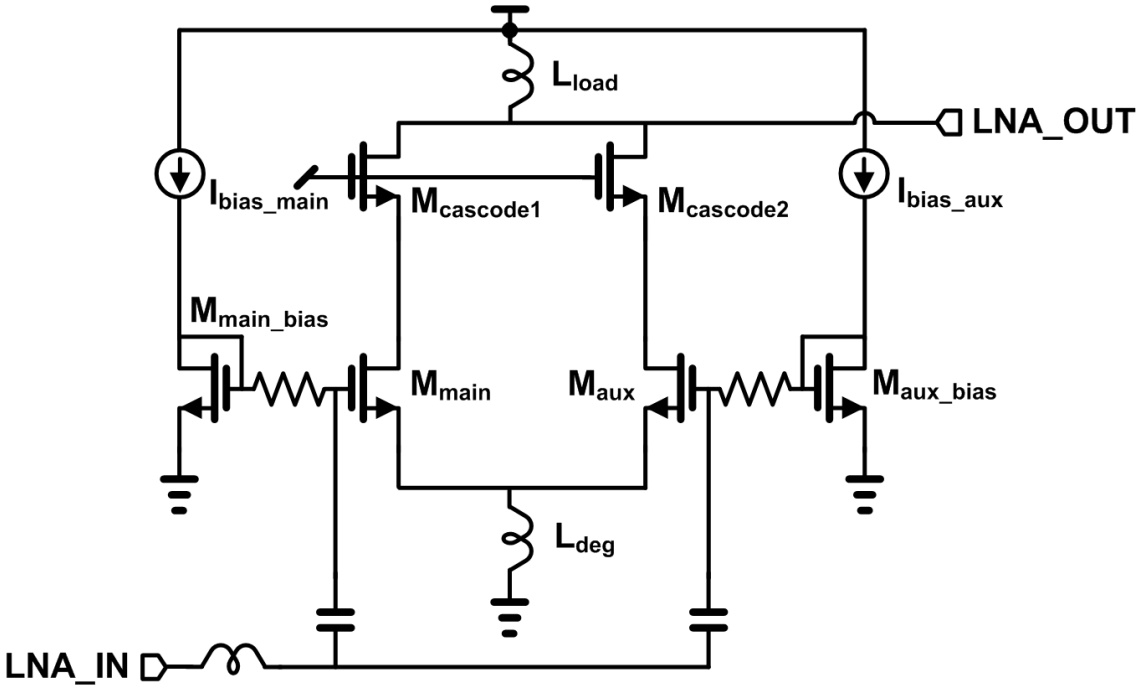

Figure 29. Schematic of the low-noise amplifier.

4.3.3.3 LO frequency divider

As the RF input signal is down-converted to the baseband quadrature signals, the quadrature LO signals are required [26]. To generate the quadrature signals, frequency divider as Figure 30 is used. The frequency divider generates balanced quadrature signals by utilizing twice frequency. The frequency divider is composed of two latches which cross coupled each other. Two dividers are used for the RX LO and the TX LO. In the real system application, a voltage-controlled oscillator (VCO) is connected to the LO divider.

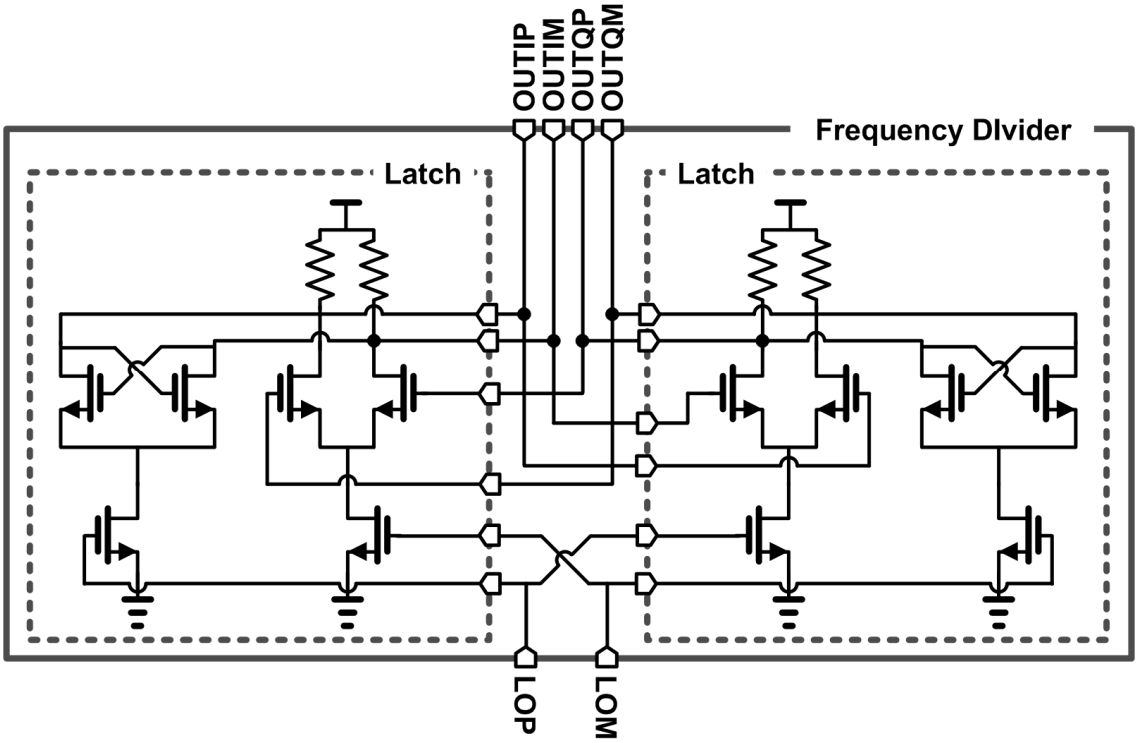

Figure 30. Schematic of the LO frequency divider.

4.3.3.4 TX canceller

The schematic of the TX canceller part is shown as Figure 31. The LNA output is fed to the down-conversion mixer which is made by a passive mixer to reduce the power consumption and improve the linearity. Then, the TX leakage signal passes through the first-order LPF followed by the up-conversion single-sideband mixer. As the RX signal is filtered at the LPF, active mixer can be employed after the LPF. The output common-mode voltage of the LPF is set for the up-conversion mixer to have a desired bias current. A simple RC filter is also used the up-conversion mixer to attenuate the RX signal further.

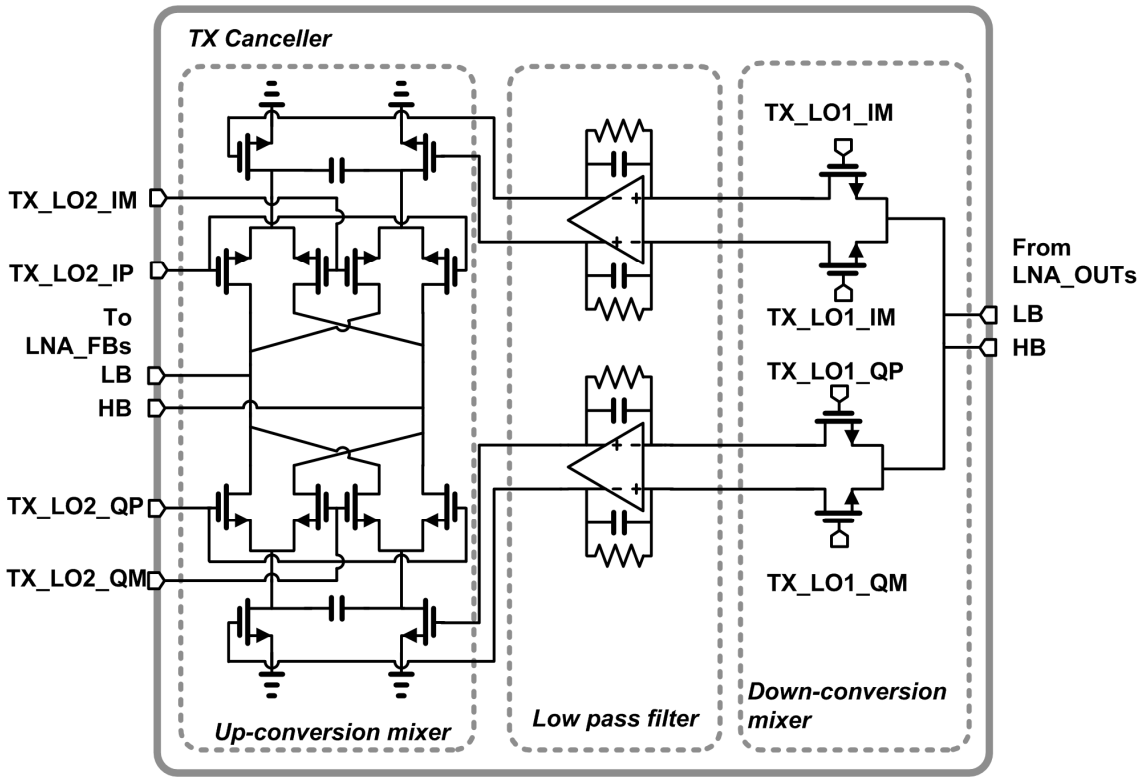

Figure 31. Schematic of the TX canceller.

4.3.4 Simulation result

The RF front-end is designed using a 0.18-μm CMOS process. The open loop and closed loop characteristics of the low-band LNA and the high-band LNA are shown in Figure 32 and 33, respectively. As the loop gain crossed the 0-dB line at two points, phase margin was investigated at these two points. Changing the LO phase with the phase shifter achieved the maximum phase margin. Although the TX attenuations near the TX LO frequency were not changed by the loop phase in the closed loop response, peaking indicates the lack of phase margin.

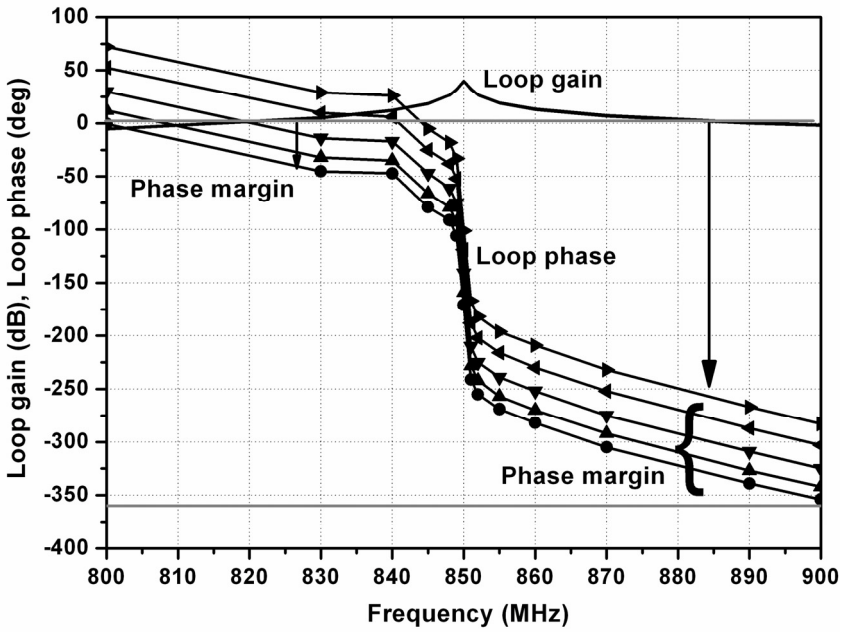

(a)

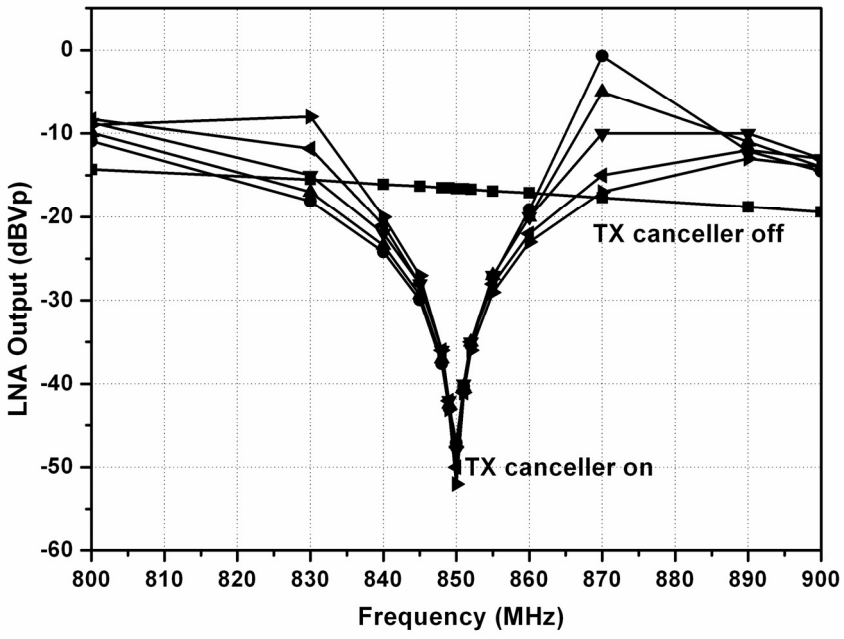

(b)

Figure 32. Frequency response of the low-band LNA, (a) loop gain and phase of the feedback loop, (b) the closed loop response.

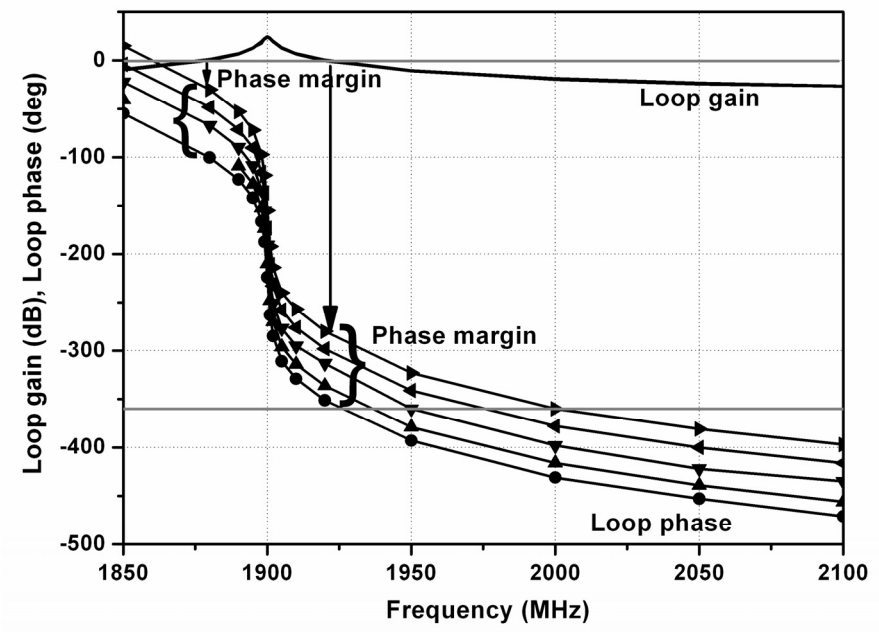

(a)

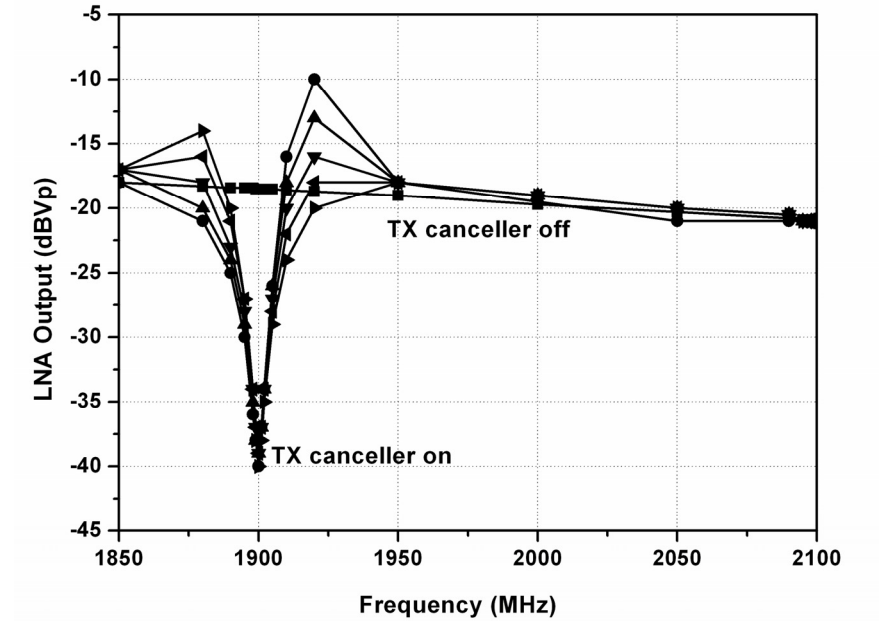

(b)

Figure 33. Frequency response of the high-band LNA, (a) loop gain and phase of the feedback loop, (b) the closed loop response.

The frequency response of the total receiver was also simulated as shown in Figure 34. 30-dB notches were observed because of the proposed TX leakage cancellation. The NFs of the LNAs were also simulated.

The NF degradation for the low-band LNA and the high-band LNA were 1.2-dB and 0.4-dB, respectively. However, those degraded NFs were still within the specifications. The NFs of the total receivers were simulated. In the low frequency below 10-Hz, the NFs were increased due to the flicker noise effect of the TIA following the RX mixers. However, the flicker noise power does not dominate the total noise power over the channel. When the TX canceller was inactivated, the total NFs of the low-band and the high-band receivers were 1.4dB. When the TX canceller was activated, the total NFs were increased to 2.1dB for the low-band and 1.9dB for high band, respectively.

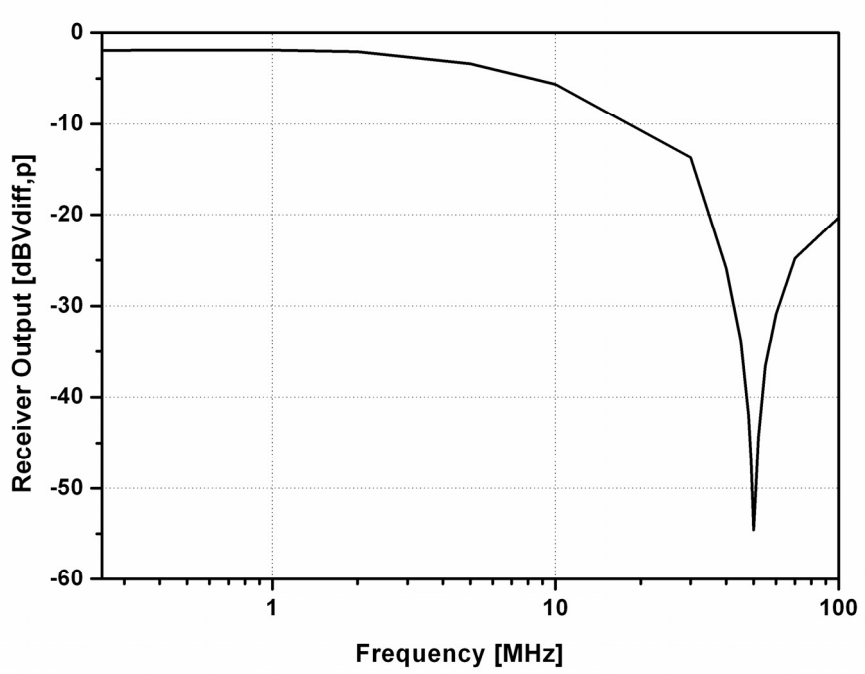

(a)

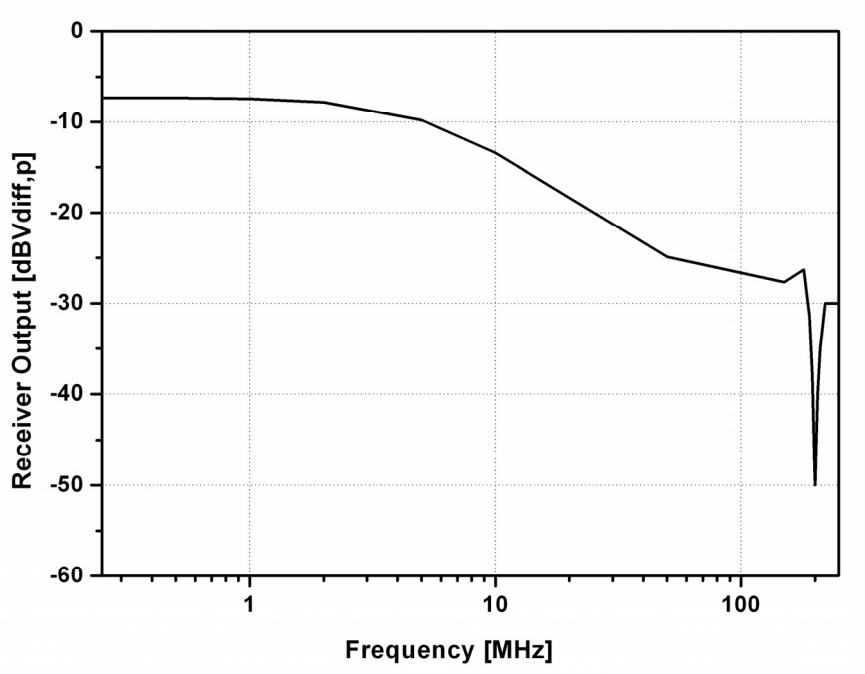

(b)

Figure 34. Frequency response of the total receiver, (a) low-band, (b) high-band.

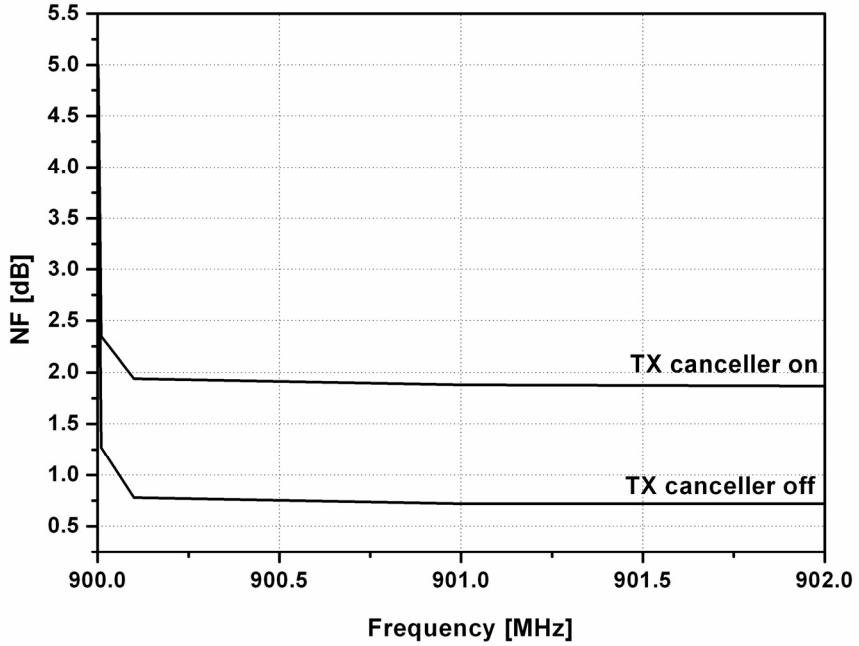

(a)

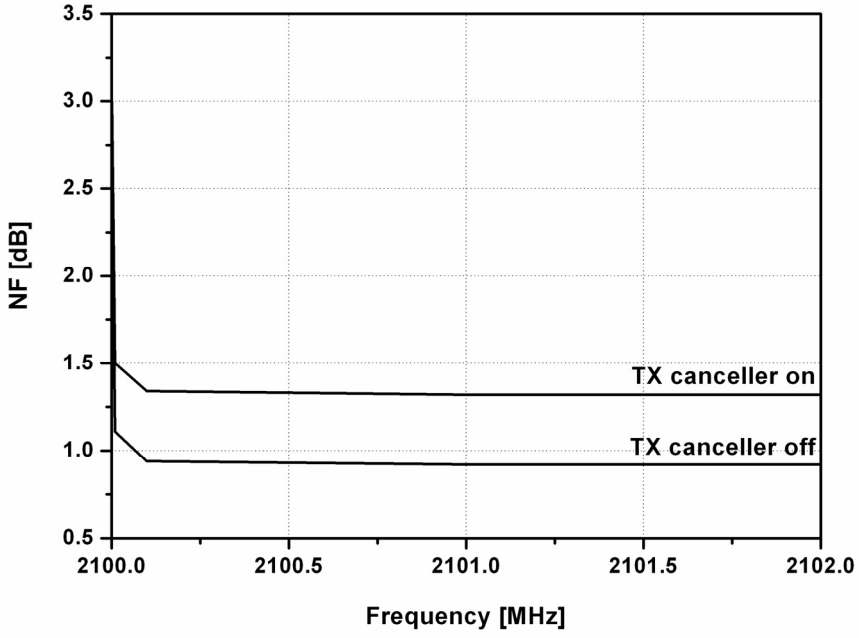

(b)

Figure 35. Noise figure of the LNAs, (a) low-band, (b) high-band.

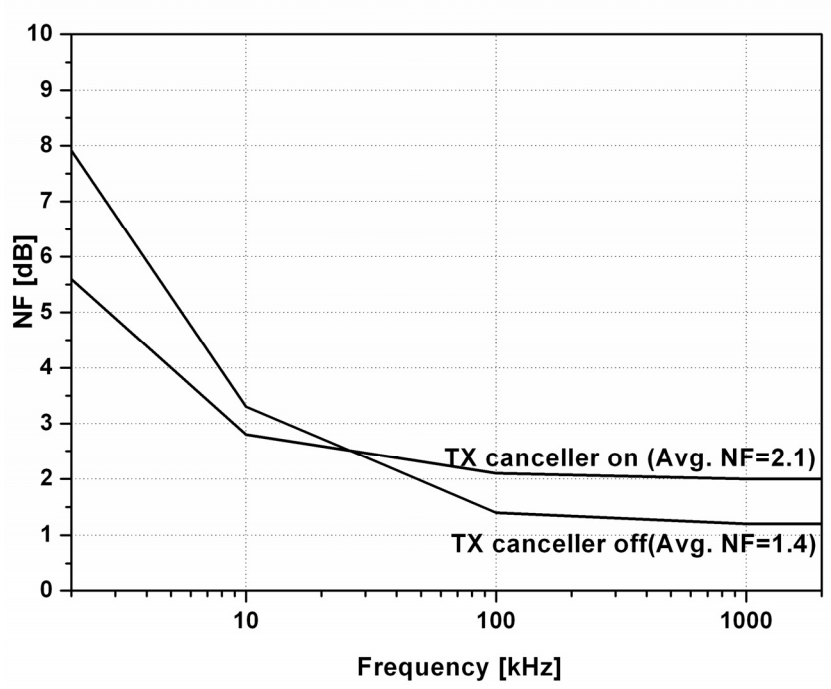

(a)

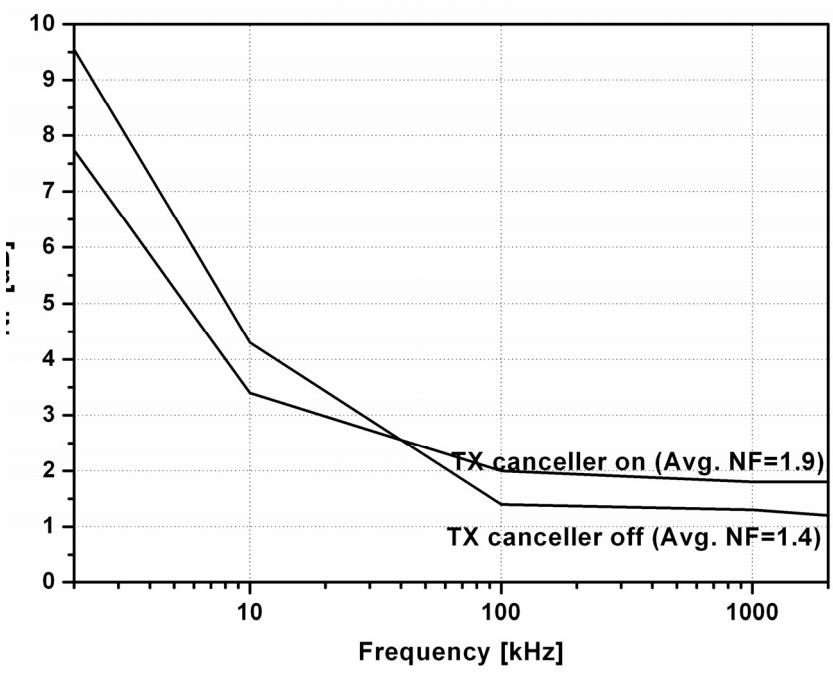

(b)

Figure 36. Noise figure of the total receiver, (a) low-band, (b) high-band.

4.3.5 Implementation and measured result

The proposed SAW-less receiver was implemented using a 0.18-μm CMOS process in 2.2 mm^2 as Figure 37. Figure 38 shows the measurement setup for the SAW-less receiver. Agilent® E4438C ESG signal generators were used to apply RF single tone or WCDMA modulated signal to the LNA input [27]. The chip is controlled by the I^2C serial bus interface, and an interface board is used to send the I^2C command to the chip via USB cable.

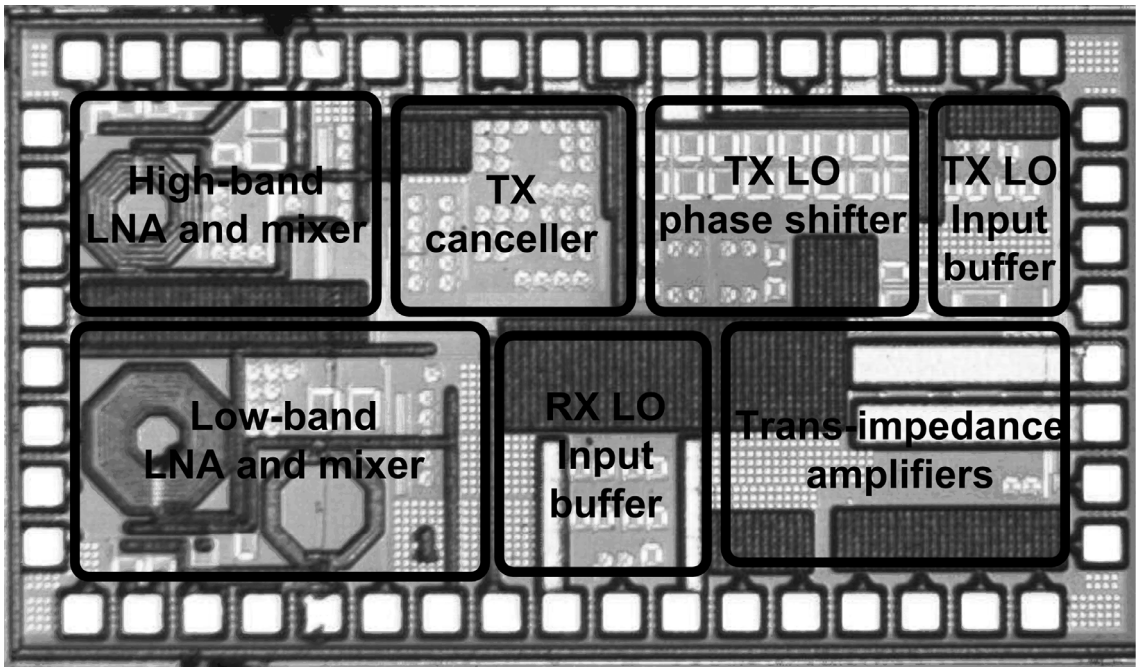

Figure 37. Microphotograph of the chip.

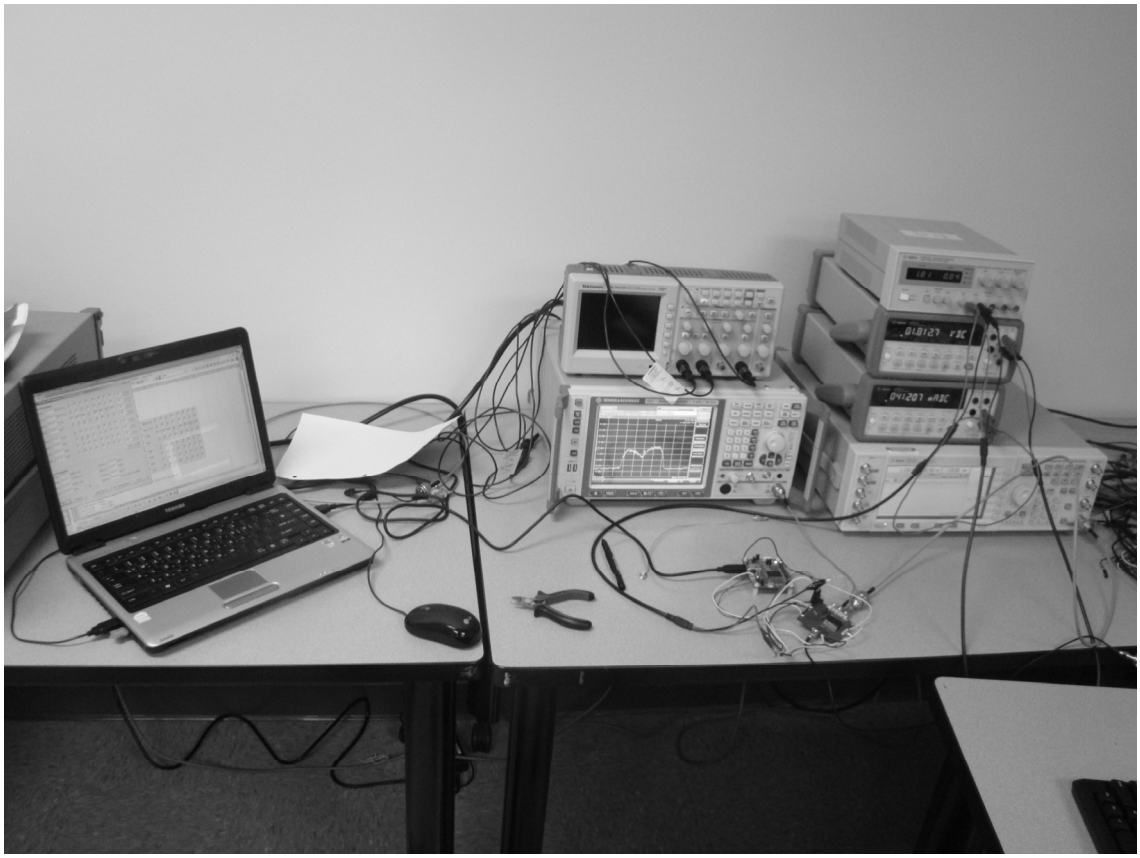

Figure 38. Measurement setup.

Figure 39 shows the TX leakage cancellation using a sinusoidal single tone for the low-band LNA and the high-band LNA, respectively. When the TX canceller was active, the TX LO signal was detected at the LNA output. The main source of the TX LO leakage is the mismatch between two balance signals and the substrate coupling. To reduce the TX LO leakage, the block placement and symmetric layout are highly required. The TX leakage attenuations of 17-dB and 20-dB were achieved for the low band and high band, respectively.

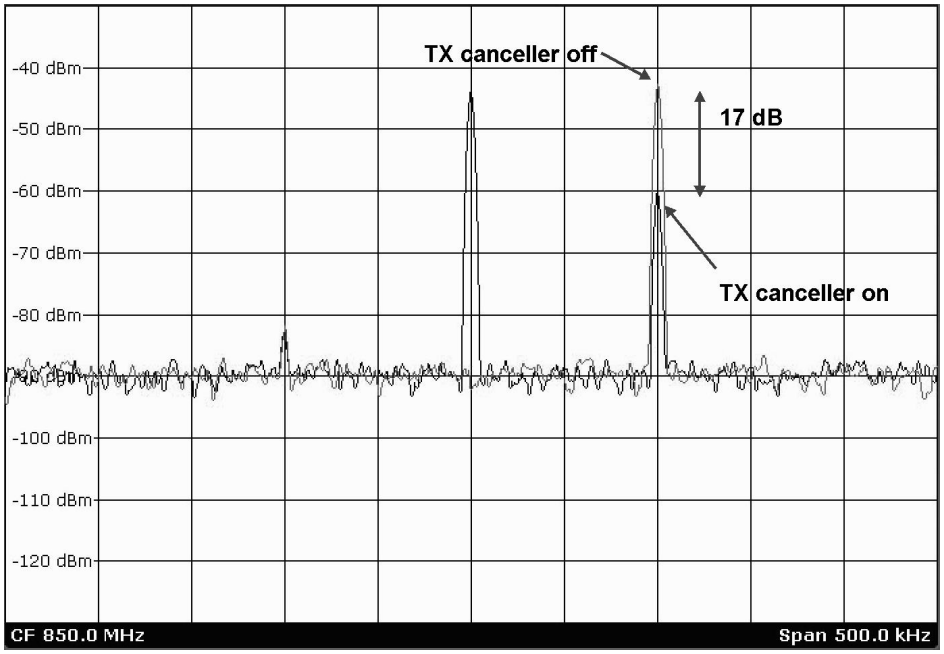

(a)

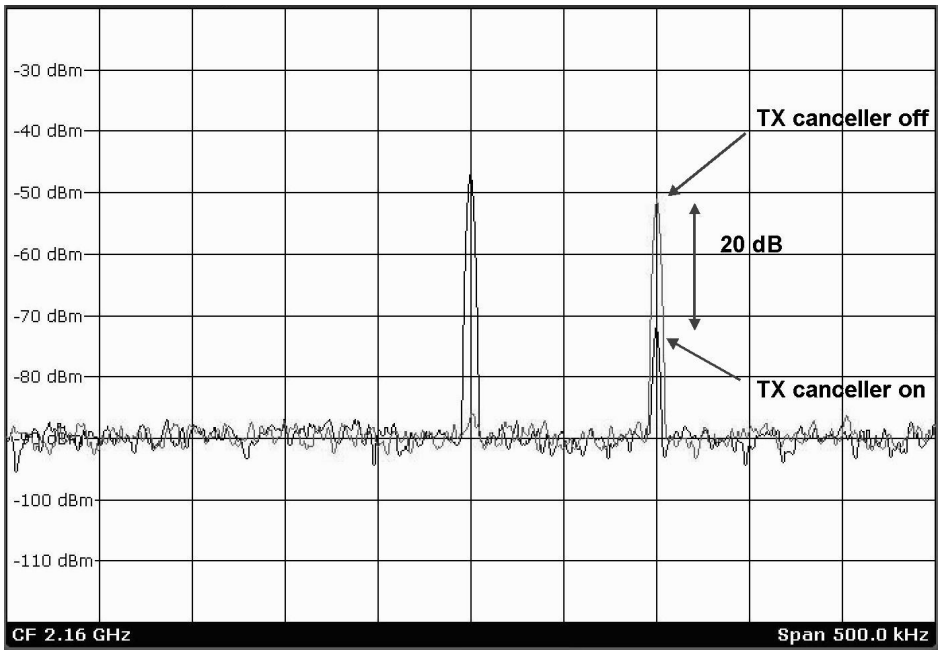

(b)

Figure 39. LNA output spectrum with the TX leakage cancellation on and off (a) low band, (b) high band.

The TX leakage cancellation for an entire WCDMA signal was evaluated by applying a WCDMA signal to the LNA input and measuring it at the LNA output. As shown in Figure 40, the TX canceller is effective for the modulated signal as well. The notch shape was visible when the WCDMA modulated signal is applied because the feedback loop gain is the largest at the TX LO frequency.

To evaluate the phase rotator for the multi-band application, the TX leakage attenuation was measured using WCDMA signal with the change of the LO phase as shown in Figure 41. As the phase of the LO changed, the amount of the attenuation and the attenuated waveform changed. When the phase margin is not sufficient, peaking is observed as expected by the design. Figure 42 shows the frequency response of the low-band and the high-band LNAs at the optimal TX canceller phase. The total frequency responses of the receiver were also measured as shown in Figure 43 for the low-band and the high-band. The notch is found at the offset frequency between the RX and the TX signals.

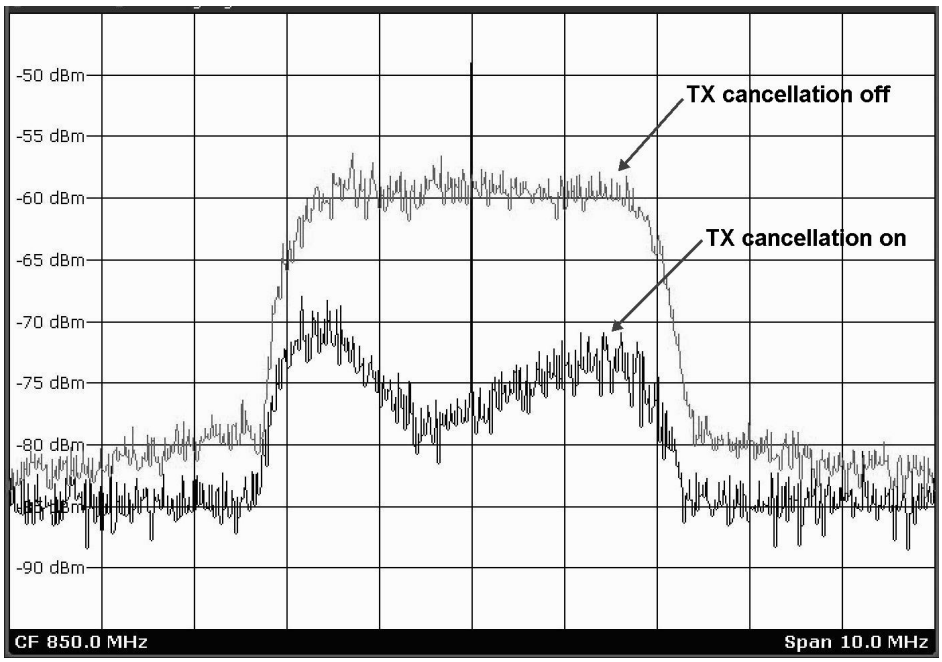

(a)

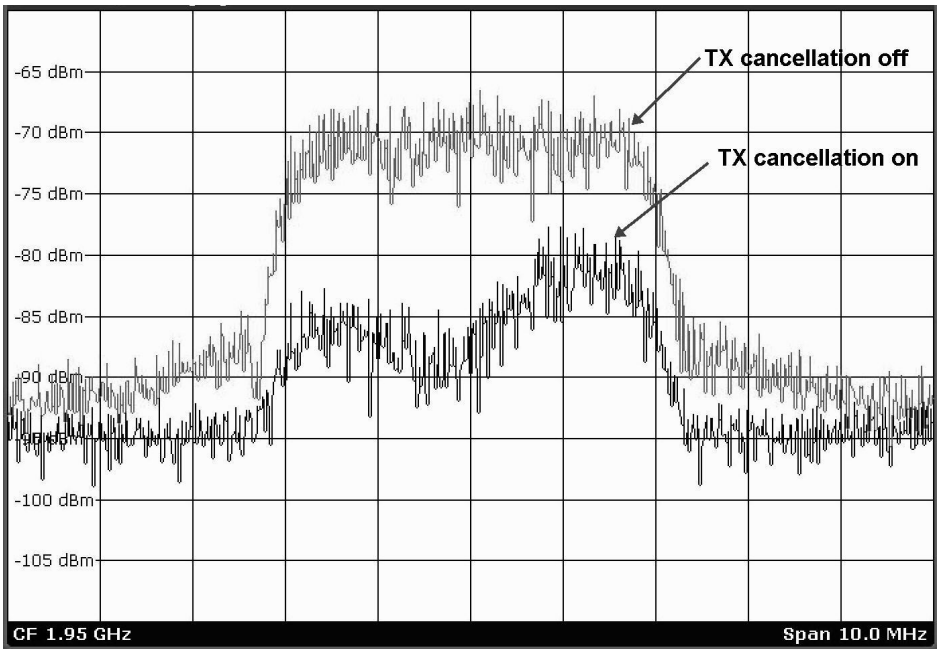

(b)

Figure 40. LNA output spectrum with WCDMA modulated signal with the TX cancellation on/off, (a) low band, (b) high band.

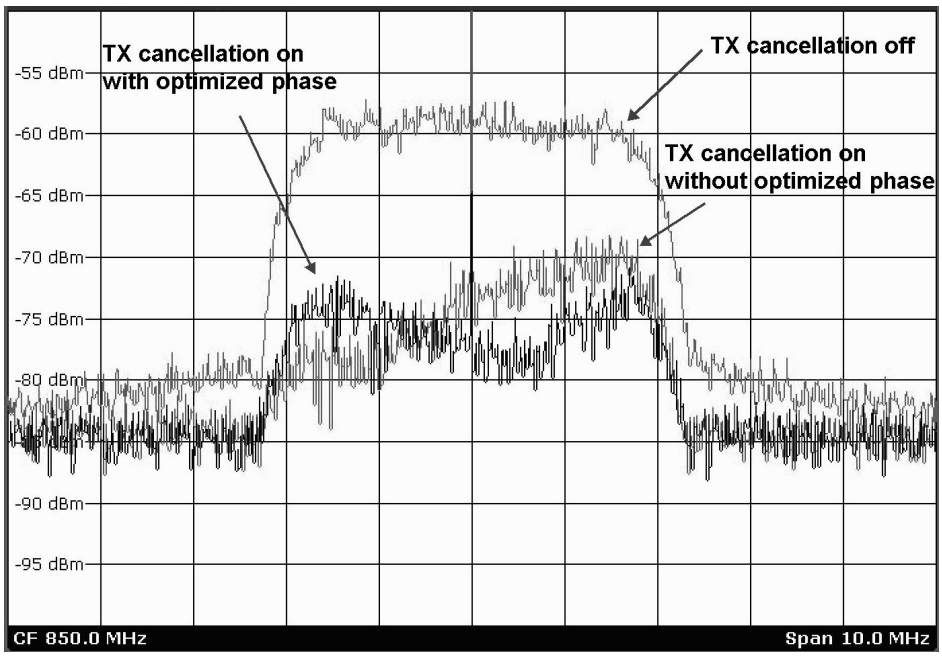

(a)

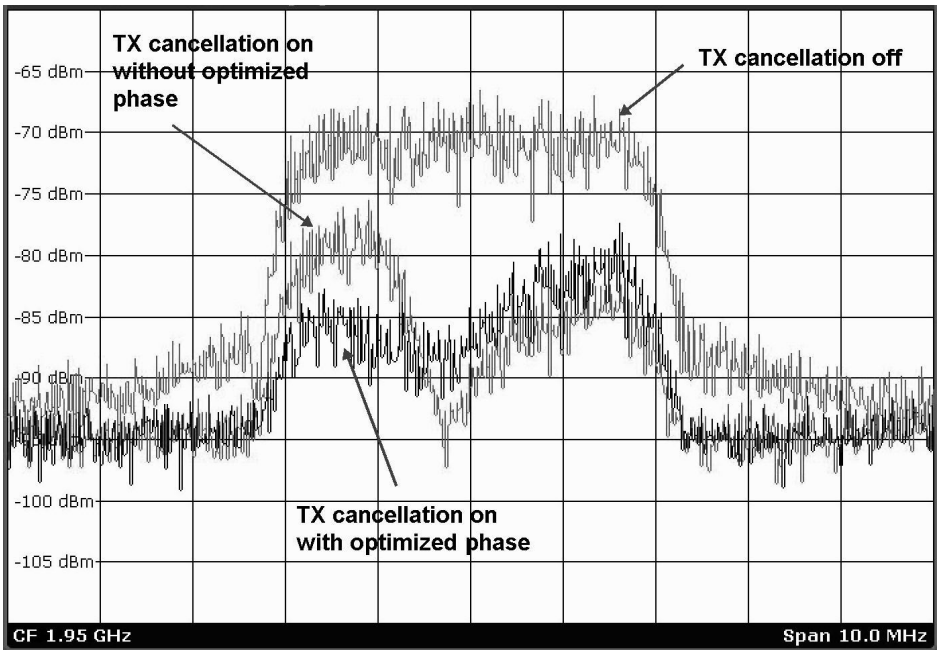

(b)

Figure 41. LNA output spectrum with WCDMA modulated signal by changing phase of the LO phase rotator, (a) low band, (b) high band.

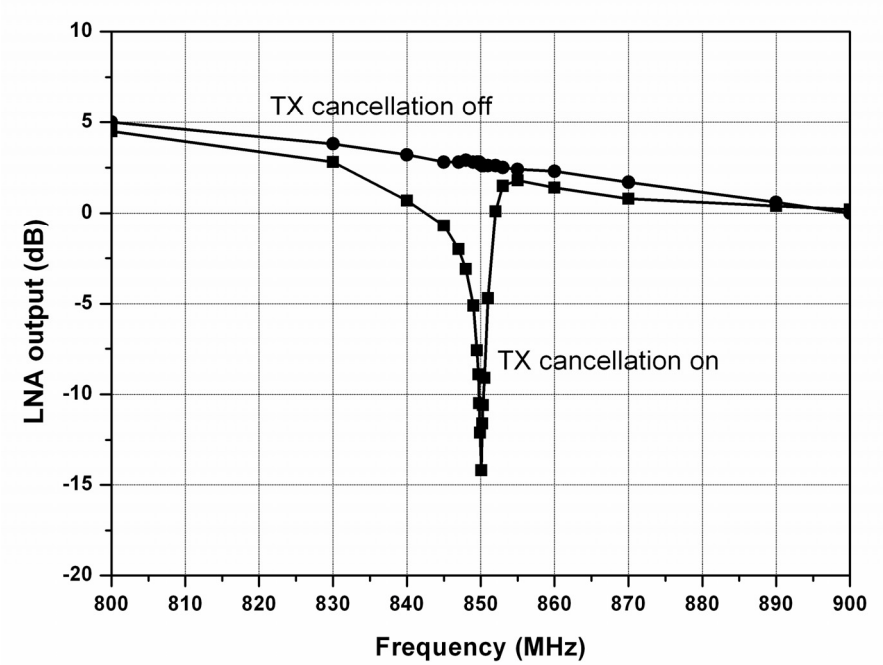

(a)

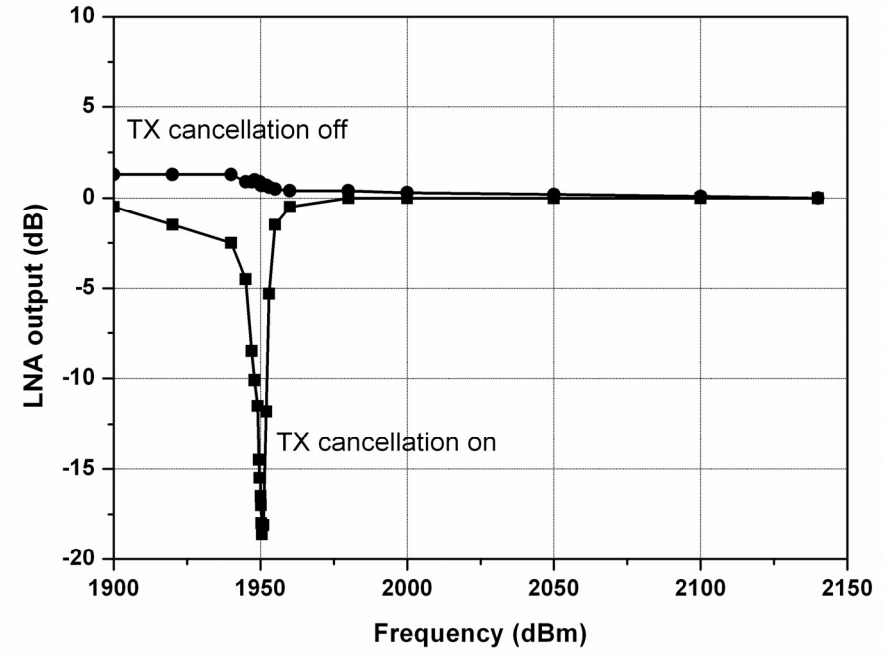

(b)

Figure 42. LNA frequency response, (a) low band, (b) high band.

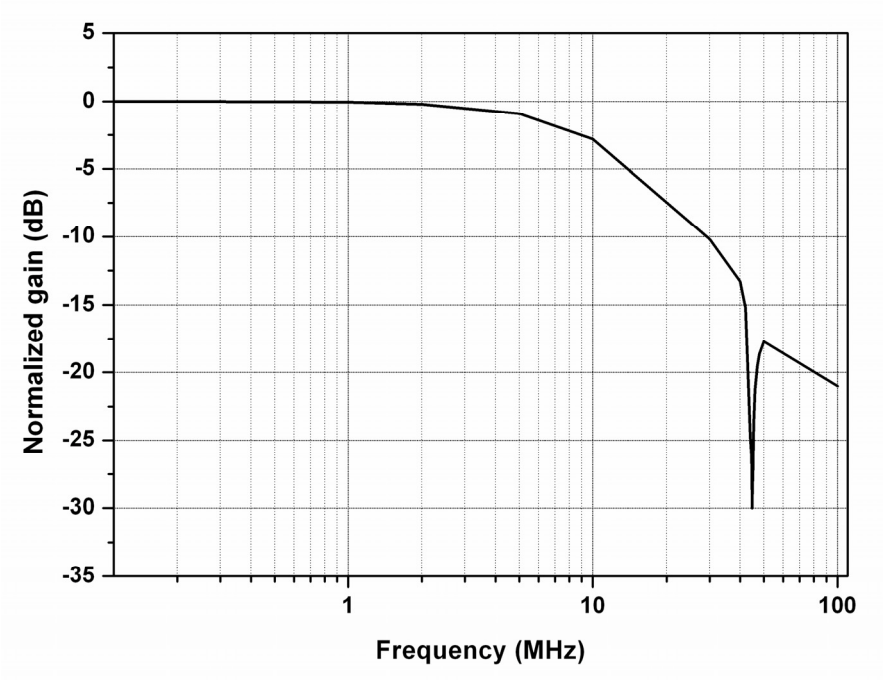

(a)

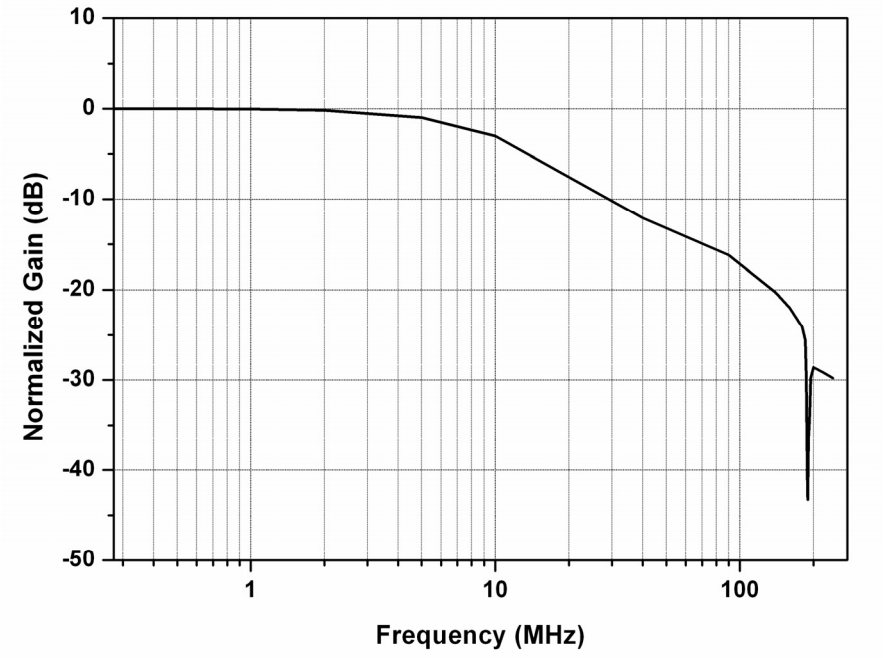

(b)

Figure 43. Total receiver frequency response, (a) low band, (b) high band.

The measured performance is summarized in Table 10. The performance is also compared with previous SAW-less receivers. The receiver chip with the proposed technique achieved the highest TX leakage attenuation while achieving comparable NF degradation and the current consumption. In addition, the multi-band application technique is proposed for the first time using shared TX canceller to reduce the silicon area. The 96% of the TX canceller current consumed at the LO phase shifter which dose not considered previously. It must be expressed that the TX leakage cancellation of [12] has a potential problem of the uncertainty by providing the feedback signal to the duplexer port.

Table 10. Current breakdown by blocks (mA).

Block		LB	HB
Receiver	LNA	8.9	11.3
	Mixer	0	0
	TIA	6.1	6.1
	Receiver total	15	17.4
TX canceller	TX Canceller	0.34	0.34
	LO phase rotator	9.2	9.2
	TX canceller total	9.5	9.5
SAW-less receiver total		24.5	26.9

Table 11. Performance receiver comparison to previous works.

		[11]	[12][a]	This work	
				LB	HB
Block		LNA Mixer	LNA	LNA + Mixer	
Gain	dB	45	19.9	30.4	27.8
NF[b]	dB	3.1/4.8	1.5/1.7	1.8/2.4	2.1/2.6
Tx Att.	dB	6	18	17	20
Current	mA	30/53	11/15	15/24.5	17.4/26.9

a) Feedback loop uncertainty, b) TX canceller off/on

4.4 CONCLUSIONS

In this chapter, new methods for TX leakage cancellation for a WCDMA receiver are presented. Required TX leakage attenuation, more than 20-dB, was delivered from the WCDMA standard, and frequency-selective feedback was used to accomplish this TX leakage attenuation. By completing the feedback loop inside the chip, the feedback loop characteristic became predictable and insensitive to the duplexer impedance. To support multi-band, a LO phase shifter was also proposed to achieve maximum phase margin for each band. The proposed receiver was implemented using a 0.18-μm CMOS process. The measured results met the standard specifications and demonstrated the effectiveness of the proposed technique.

CHAPTER 5

TECHNICAL CONTRIBUTIONS OF THE DISSERTATION

Over the last twenty years, wireless communication applications have been flourishing. Recently, more functionality has been merged into a single mobile device in various frequency bands. As a result, a multi-band multi-standard receiver is highly needed. In this dissertation, several new architectures are presented to achieve a multi-band multi-standard receiver that can be produced at low cost and consumes low power.

The technical contributions of this dissertation can be summarized as follows. First, the required receiver performance is derived from the WCDMA specification. Second, based on the receiver performance, the required TX attenuation is obtained. Third, frequency selective feedback architecture is proposed with the insensitivity in the receiver input port impedance to realize the required TX attenuation. Fourth, a technique to shift the phase of the feedback loop is proposed for the TX cancellation to become applicable to multi-band. Fifth, for multi-standard applications, a novel resistor bank topology is proposed for an active-RC channel-selection filter to achieve pseudo-continuous bandwidth tuning and fine gain steps. Sixth, dual-common-mode feedback two-stage amplifier is proposed to reduce the power consumption of the channel-selection filter according to the channel environment. These technological improvements will allow for the creation of a low-power multi-band multi-standard receiver with the TX leakage cancellation capability at a low cost.

REFERENCES

[1] Universal Mobile Telecommunications System (UMTS); User Equipment (UE) conformance specification; Radio transmission and reception (FDD); Part 1: Conformance specification (3GPP TS 34.121-1 version 8.8.0 Release 8).

[2] Mobile and Portable DVB-T Radio Access Interface Specification, European Industry Association EICTA, MBRIA-02-16, Version 1.0.

[3] Digital Audio Broadcasting (DAB): Signal strengths and receiver parameters; Targets for typical operation, ETSI TS 101 758 V1.1.1 (2000-07).

[4] H. Amir-Aslanzadeh, E. J. Pankratz, and E. Sanchez-Sinencio, "A 1-V +31 dBm IIP3, Reconfigurable, Continuously Tunable, Power-Adjustable Active-RC LPF," *Solid-State Circuits, IEEE Journal of,* vol. 44, no. 2, pp. 495-508, Feb. 2009.

[5] A. Vasilopoulos, G. Vitzilaios, G. Theodoratos, and Y. Papananos, "A Low-Power Wideband Reconfigurable Integrated Active-RC Filter With 73 dB SFDR," *Solid-State Circuits, IEEE Journal of,* vol. 41, no. 9, pp. 1997-2008, Sept. 2006.

[6] M. T. Ozgun, Y. Tsividis, and G. Burra, "Dynamic Power Optimization of Active Filters With Application to Zero-IF Receivers," *Solid-State Circuits, IEEE Journal of,* vol. 41, no. 6, pp. 1344-1352, June 2006.

[7] Avago Technologies FBAR duplexer: ACMD 7612. Datasheet online available at http://www.avagotech.com/docs/AV02-0473EN.

[8] D. Morgan, *Surface Acoustic Wave Filters: With Applications to Electronic Communication and Signal Processing*, 2nd ed. Academic Press, 2007.

[9] Epcos SAW filter: B9411. Datasheet online available at http://www.epcos.com/inf/40/ds/mc/B9411.pdf.

[10] H. Darabi, "A Blocker Filtering Technique for SAW-Less Wireless Receivers," *Solid-State Circuits, IEEE Journal of,* vol. 42, no. 12, pp. 2766-2773, Dec. 2007.

[11] H. Khatri, P. S. Gudem, L. E. Larson, "An Active Transmitter Leakage Suppression Technique for CMOS SAW-Less CDMA Receivers," *Solid-State Circuits, IEEE Journal of,* vol. 45, no. 8, pp. 1590-1601, Aug. 2010.

[12] V. Aparin, "A New Method of TX Leakage Cancellation in W/CDMA and GPS Receivers," in *IEEE Radio Frequency Integrated Circuits Symposium,* 2008, pp. 87-90.

[13] J. Tow, "Active RC Filters—A State-Space Realizations," *Proc. IEEE (Lett.),* vol. 56, pp. 1137-1139, June 1968.

[14] L. C. Thomas, "The Biquad: Part I—Some Practical Design Considerations," *Circuit Theory, IEEE Transaction on,* vol. CT-18, no. 3, pp. 350-357 May 1971.

[15] A. Springer, L. Maurer, R. Weigel, "RF System Concepts for Highly Integrated RFICs for W-CDMA Mobile Radio Terminals," *Microwave Theory and Techniques, IEEE Transactions on,* vol. 50, no. 1, pp. 254-267, Jan. 2002.

[16] RFMD power amplifier: RF3267. Datasheet online available at http://www.rfmd.com/CS/Documents/3267DS.pdf.

[17] J. Zipper, R. Vazny, L. Maurer, M. Wilhelm, T. Greifeneder, A. Holm, "A Single-Chip Dual-Band CDMA2000 Transceiver in 0.13μm CMOS," in *IEEE International Solid-State Circuits Conference,* 2007, pp. 342-343.

[18] B. Razavi, *RF Microelectronics*, Upper Saddle River, NJ: Prentice Hall, 1998.

[19] J. Crols, M. S. J. Steyaert, "A 1.5GHz Highly Linear CMOS Downcoversion Mixer," *Solid-State Circuits, IEEE Journal of,* vol. 30, no. 7, pp. 736-742, F 1995.

[20] L. Der, B. Razavi, "A 2-GHz CMOS Image-Reject Receiver With LMS Calibration," *Solid-State Circuits, IEEE Journal of,* vol. 38, no. 2, pp. 167-175, Feb. 2003.

[21] A. Aparin, L. E. Larson, "Modified Derivative Superposition Method for Linearizing FET Low-Noise Amplifiers," *Microwave Theory and Techniques, IEEE Transactions on*, vol. 53, no. 2, pp. 571-581, Feb. 2005.

[22] N. Kim, V. Aparin, K. Barnett, C. Persico, "A Cellular-Band CDMA 0.25-μm CMOS LNA Linearized Using Active Post-Distortion," *Solid-State Circuits, IEEE Journal of,* vol. 41, no. 7, pp. 1530-1534, July 2006.

[23] N. Poobuapheun, W.-H. Chen, Z. Boos, A. M. Niknejad, "A 1.5-V 0.7-2.5-GHz CMOS Quadrature Demodulator for Multiband Direct-Conversion Receivers," *Solid-State Circuits, IEEE Journal of,* vol. 42, no. 8, pp. 1669-1677, Aug. 2007.

[24] W. Redman-White, D. M. W. Leenaerts, "1/f noise in passive CMOS mixers for low and zero IF integrated receivers," in *European Solid-State Circuits Conference, IEEE proceeding of*, pp. 41-44, 2001.

[25] S. Zhou, M. -C. F. Chang, "A CMOS passive mixer with low flicker noise for low-power direct-conversion receiver," *Solid-State Circuits, IEEE Journal of,* vol. 40, no. 5, pp. 1084-1093, May 2005.

[26] S. Pellerano, S. Levantino, C. Samori, A. L. Lacaita, "A 13.5-mW 5-GHz Frequnecy Synthesizer With Dynamic-Logic Frequency Divider," *Solid-State Circuits, IEEE Journal of,* vol. 39, no. 2, pp. 378-383, Feb. 2004.

[27] Agilent Vector Signal Generator: E4438C. Datasheet online available at http://www.home.agilent.com/agilent/product.jspx?cc=US&lc=eng&nid=-536902340.536880956&pageMode=SP.

PUBLICATIONS

[1] **S. Beck**, S. Jeong, S. Min, M.-W. Hwang, S. T. Kim, K. Lim, and E. M. Tentzeris, "A 0.5 – 6 MHz Active-RC LPF with Fine Gain Steps Using Binary Interpolated Resistor Banks," accepted in *IEICE Transactions on Electronics*.

[2] **S. Beck,** S. T. Kim, M. Lee, K. Lim, J. Laskar, and M. M. Tentzeris, "A New Power-Consumption Optimization Technique for Two-Stage Operational Amplifiers," accepted in *IEICE Transactions on Electronics*.

[3] **S. Beck**, S. T. Kim, K. Lim, and M. M. Tentzeris, "A Multi-Band WCDMA SAW-Less Receivers with Frequency Selective Feedback Loop," accepted in *IEEE Midwest Symposium on Circuits and Systems*, 2011.

[4] **S. Beck**, H.-S. Kim, K. Chae, K. Lim, J. Laskar, and M. M. Tentzeris, "A Multi-Band WCDMA SAW-Less Receivers with Frequency Selective Feedback Loop," under review in *IEEE Transactions on Microwave Theory and Technique*.

[5] S. T. Kim, **S. Beck**, T. Song, K. Kim, and J. Laskar, "Subthreshold Current Mode Matrix Determinant Computation for Analog Signal Processing," in *IEEE International Symposium on Circuits and Systems*, May 2010 pp. 1260 - 1263.

[6] M. Lee, **S. Beck**, K. Lim, and J. Laskar, "Analog Auto-Correlation Based Receiver Architecture for Radar Systems," in *Military Communications Conference,* 2010.

[7] K.-S. Lee, **S. Beck**, H. Jeon, Y. Yoon, C.-H. Lee, and J. Kenney, "A 45nm SOI-CMOS PLL with a Wideband LC-VCO," accepted in *IEEE Midwest Symposium on Circuits and Systems*, 2011.

[8] S. T. Kim, K. Chae, J. Choi, **S. Beck,** S. Kim, F. Bien, C. Lee, K. Lim, J. Laskar, and M. M. Tentzeris, "A Non-Interruptive Link-Variation Monitoring Circuit for Wireless Sensor Applications," under review in *IEEE Microwave and Wireless Components Letters.*

VITA

Sungho Beck received a B.S. and an M.S. in electrical engineering from the Korea Advanced Institute of Science and Technology in Daejon, Korea, in 1999 and 2001, respectively. He has been working toward a Ph.D in electrical and computer engineering at the Georgia Institute of Technology in Atlanta, Georgia, since 2008. From 2001 to 2008, he was involved in the development of transceivers for Future Communications IC (FCI), Inc. (Currently, Silicon Motion Technology) in Sungnam, Korea. From 2011, he has been working for Texas Instruments in Dallas, Texas, where he is developing power-management IC. His current research interests include the design of analog and mixed-signal ICs such as linear voltage regulators, switching-mode power supply, and wireless-communication transceivers.